


Research Article

Influences of sea level changes and the South Asian Monsoon on southern Red Sea oceanography over the last 30 ka

Spyros Sergiou^{a*} , Maria Geraga^a, Eelco J. Rohling^{a,c}, Laura Rodríguez-Sanz^b, Ekaterini Hadjisolomou^{a,d}, Francesca Paraschos^{a,e}, Dimitris Sakellariou^e and Geoffrey Bailey^{f,g}

^aLaboratory of Marine Geology and Physical Oceanography, Department of Geology, University of Patras, Patras 26504, Greece; ^bResearch School of Earth Sciences, Australian National University, Canberra, ACT, 2601, Australia; ^cOcean and Earth Science, University of Southampton, National Oceanography Centre, Southampton, SO14 3ZH, United Kingdom; ^dDepartment of Electrical Engineering and Computer Engineering and Informatics, Cyprus University of Technology, 30 Arch. Kyprianos Str., 3036 Limassol, Cyprus; ^eInstitute of Oceanography, Hellenic Centre for Marine Research, 19013 Anavyssos, Greece; ^fDepartment of Archaeology, King's Manor, University of York, York, YO1 7EP, United Kingdom and ^gCollege of Humanities, Arts and Social Sciences, Flinders University, Adelaide, SA 5001, Australia

Abstract

The southern Red Sea is a key region for investigating the effect of climate forces on a semi-closed basin. Detailed micropaleontological (planktic foraminifera) and isotopic ($\delta^{18}\text{O}$, $\delta^{13}\text{C}$) analyses along with reconstructions of sea surface temperature and salinity on a sediment core from the Farasan banks revealed the imprints of sea level changes and the South Asian Monsoon on the area. Comparison with surrounding records provided insights on the Red Sea–Gulf of Aden (GoA)–Northwestern Arabian Sea (NWARs) water exchange pattern over the last 30 ka. During glacial sea-level lowstand, flow of water from the GoA prevented hypersalinity in the southern Red Sea. Deglacial sea level rise improved water mass exchange between the NWArS, GoA and the entire Red Sea, resulting in relatively similar surface water conditions during the early Holocene when sea-level rise slowed. Thus, sea level change is the major driver of Red Sea $\delta^{18}\text{O}$ variability. Southwest Monsoon (SWM), which was dominant during the late glacial and Early–Middle Holocene, enhanced surface productivity in the southern Red Sea. Northeast Monsoon (NEM) dominated around Heinrich stadial 1, as indicated by a nearly planktonic zone that was probably caused by restricted GoA inflow and low productivity.

Keywords: Red Sea, Sea Level Changes, Paleoclimate, Monsoon, Paleoceanography, Planktic Foraminifera, Stable Isotopes

(Received 30 August 2021; accepted 16 March 2022)

INTRODUCTION

Records from basins with restricted connection to the open ocean provide essential information about the effect of climate-driven processes on hydrographic systems. Sediment archives from such areas document environmental alternations as composite results of the effects of long- and short-term climatic changes, the fluctuations of sea level stands, and freshwater input in the basin (i.e., Baltic Sea: Sohlenius et al., 1996; Black Sea–Marmara Sea complex: McHugh et al., 2008; Hoyle et al., 2021; Gulf of Corinth, Greece: McNeill et al., 2019). Within this context, the Red Sea is considered to be a prominent region for paleoclimatic and paleoceanographic studies (Rohling et al., 1998; Siddall et al., 2004).

The Red Sea is a narrow, semi-closed basin situated in an arid climate zone, and is connected at its southern end with the Indian Ocean via the 20-km-wide Bab el Mandeb Straits (Fig. 1a, b). On the basin-inward side of the straits lies the Hanish sill (137 m in depth), which, as the shallowest passage in the Red Sea connection

with the Gulf of Aden (GoA), is critical in regulating water dynamics in the basin and controlling the exchange of water masses between the Red Sea and northwestern Arabian Sea (NWARs) (Rohling, 1994; Rohling et al., 1998; Siddall et al., 2002; Biton et al., 2008).

Over Quaternary glacial-interglacial cycles, Red Sea environmental conditions have developed in accordance with sea level changes and the influence of Arabian Sea water masses driven by the South Asian Monsoon System (SAMS) (Locke and Thunell, 1988; Almogi-Labin et al., 1996; Hemleben et al., 1996; Rohling et al., 1998; Arz et al., 2003b). At times of full glacial stages of the last 500 ka, the sea level lowstands limited the basin's connection with the Indian Ocean (Rohling et al., 1998; Siddall et al., 2003; Lambeck et al., 2011), leading to near-isolation of the basin, which caused hypersaline conditions in the central and northern parts (Locke and Thunell, 1988; Hemleben et al., 1996; Fenton et al., 2000; Biton et al., 2008).

The SAMS operates on orbital timescales, following the Milankovitch cycles band and solar insolation intensity (Clemens and Prell, 2003; Leuschner and Sirocko, 2003; Kathayat et al., 2016). On shorter, (multi)millennial timescales, a synchronicity has been observed between abrupt climate events in the North Atlantic and the SAMS domains, implying a climatic teleconnection between the two regions (Sirocko et al., 1996;

*Corresponding author email address: sergiou@upatras.gr

Cite this article: Sergiou S, Geraga M, Rohling EJ, Rodríguez-Sanz L, Hadjisolomou E, Paraschos F, Sakellariou D, Bailey G (2022). Influences of sea level changes and the South Asian Monsoon on southern Red Sea oceanography over the last 30 ka. *Quaternary Research* 1–19. <https://doi.org/10.1017/qua.2022.16>

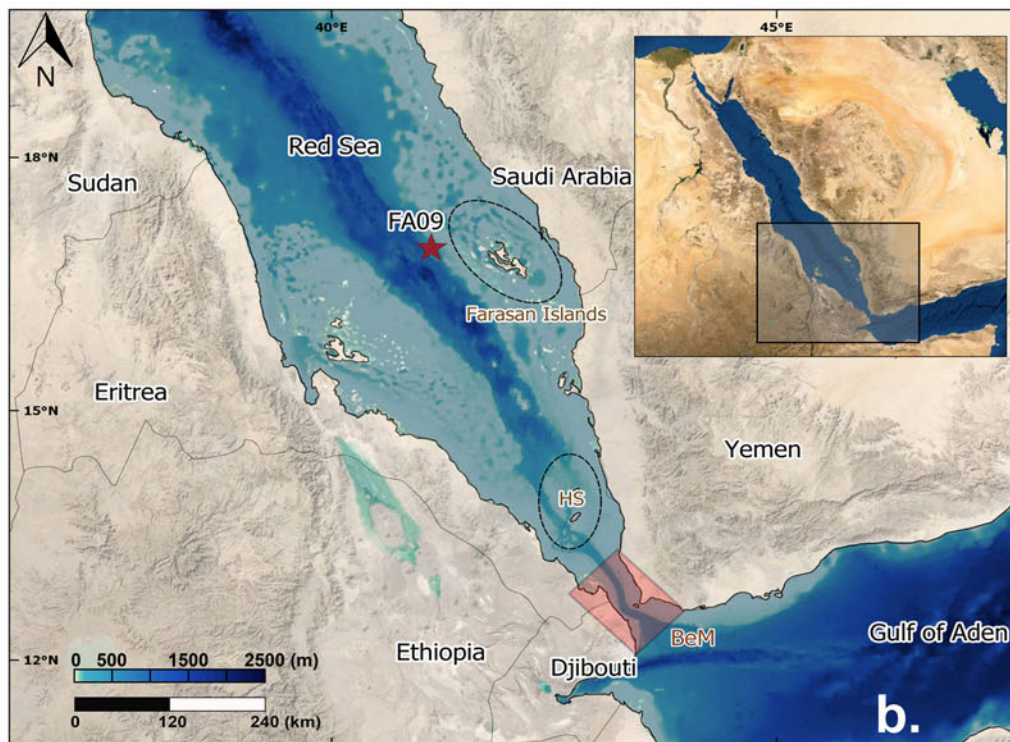
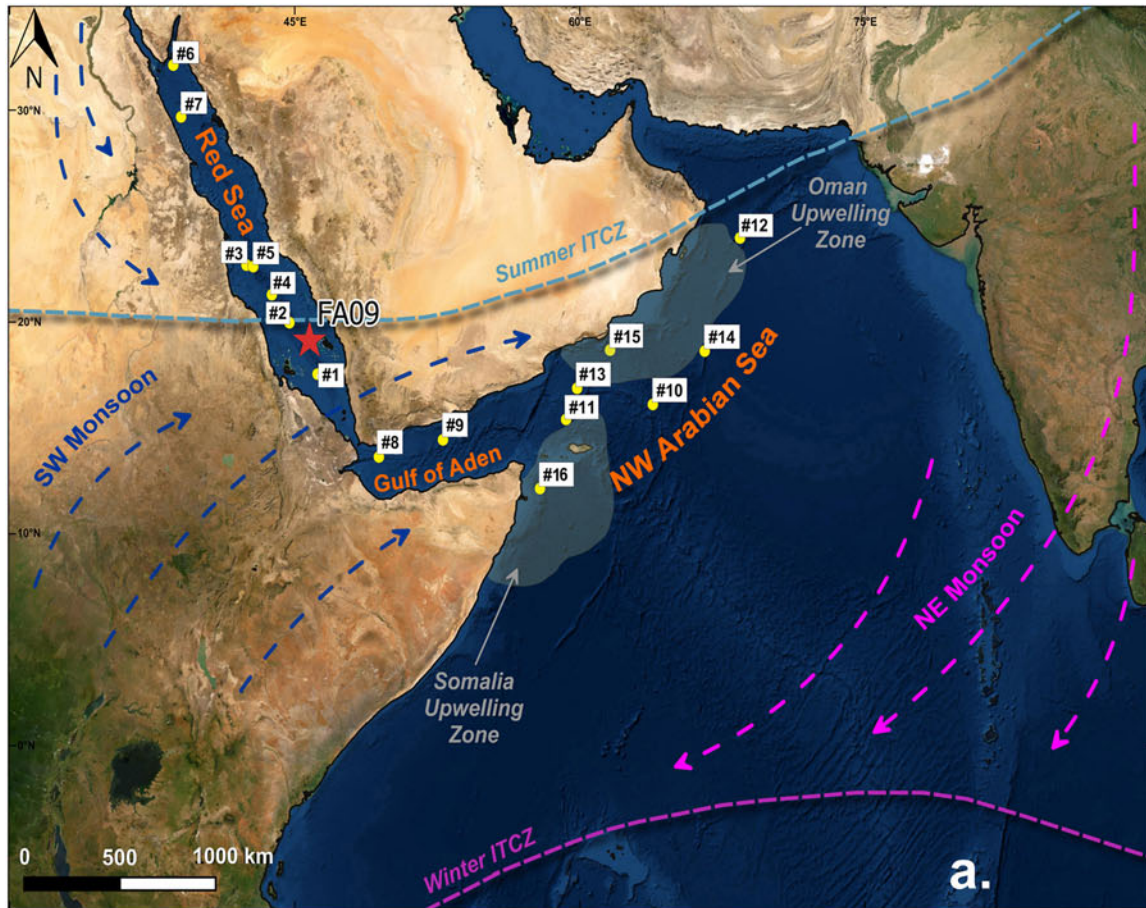


Figure 1 (a) The wider area of Red Sea, Gulf of Aden, and northwestern Arabian Sea, with the locations of the cores referred in the text (Table 1). (b) The southern Red Sea and location of FA09. The Farasan Islands archipelago and Hanish sill (HS) are indicated with elliptic shapes; the strait of Bab-el-Mandeb (BeM) is highlighted with the red rectangle.

Table 1. Sediment cores from the wider area (Fig. 1a) used for comparisons in the present study.

Region	Core Number (#)	Core Name	References
Southern Red Sea	—	FA09	This study
	1	KL32	Fenton et al., 2000; Siddall et al., 2004
	2	CH43-2	Locke and Thunell, 1988
Central Red Sea	3	KL09	Siccha et al., 2009
	4	KL11	Siddall et al., 2004; Trommer et al., 2010; Palchan and Torfstein, 2019
	5	MC91	Edelman-Furstenberg et al., 2009
Northern Red Sea	6	GeoB5844-2	Arz et al., 2003a, b; Legge et al., 2006
	7	KL23	Siddall et al., 2004
Gulf of Aden	8	RC09-166	Tierney et al., 2017
	9	KL15	Almogi-Labin et al., 2000; Palchan and Torfstein, 2019
Northwestern Arabian Sea	10	74KL	Sirocko et al., 1993
	11	NIOP929	Rostek et al., 1997; Saher et al., 2007
	12	MD2354	Böll et al., 2015
	13	GOA6	Ishikawa and Oda, 2007
	14	RC27-42	Pourmand et al., 2007
	15	GeoB3011-1	Ivanova et al., 2003
	16	NIOP905	Ivanochko et al., 2005

Schulz et al., 1998; Leuschner and Sirocko, 2000; Deplazes et al., 2013). Cool episodes in the North Atlantic, often associated with massive iceberg-discharge events and formation of ice-rafted debris (IRD) deposits (i.e., Heinrich stadials; Sanchez-Goni and Harrison, 2010), coincide with phases of southward migration of the Intertropical Convergence Zone (ITCZ), low levels of monsoonal precipitation, and dominant northeast monsoon (NEM) winds, leading to increased aridity in the Arabian Sea (Gupta et al., 2003; Ivanochko et al., 2005; Singh et al., 2011; Deplazes et al., 2014) and Red Sea (Arz et al., 2003b; Legge et al., 2006; Rohling et al., 2008; Trommer et al., 2010; Roberts et al., 2011) areas. On the other hand, millennial-scale warm and humid phases in high latitudes correspond to phases of northward displacement of the ITCZ and intensified southwest monsoon (SWM) winds, leading to high precipitation levels in the tropics (Fleitmann et al., 2007; Shakun et al., 2007). The SWM triggered upwelling of subsurface, nutrient-rich, and relatively low-temperature/salinity waters in the NWArs around the Oman and Somalia margins (Fig. 1a) (Emeis et al., 1995; Pourmand et al., 2007; Böll et al., 2015; Gaye et al., 2018).

Previous studies have employed planktic foraminifera associations for reconstructing past monsoon dynamics in the Arabian Sea (Anderson and Prell, 1991; Naidu and Malmgren, 1996; Cayre et al., 1999; Almogi-Labin et al., 2000; Schulz et al., 2002; Ivanova et al., 2003; Ishikawa and Oda, 2007; Caley et al., 2011; Singh et al., 2011, 2016). A key observation of these studies is the increased abundance of *Globigerina bulloides* (followed by *Globigerinita glutinata* and neogloboquadrinids), indicating increased upwelling and elevated productivity levels likely caused by enhanced SWM. Moreover, these elevated productivity levels were accompanied by notable reductions in the $\delta^{18}\text{O}$ and $\delta^{13}\text{C}$ records, which are interpreted as the result of intense water mixing and/or SST perturbations driven by strong SWM winds (Sirocko et al., 1993; Naidu, 2004; Saher et al., 2007; Ganssen

et al., 2011). This faunal and isotopic pattern is observed today in the upwelling regions of the Arabian Sea during the SWM season (Kroon and Ganssen, 1989; Conan and Brummer, 2000; Peeters et al., 2002; Schiebel et al., 2004).

The large majority of the investigated Red Sea records are distributed in the central and northern sectors of the basin (Reiss et al., 1980; Almogi-Labin et al., 1991, 1996; Hemleben et al., 1996; Rohling et al., 1998; Arz et al., 2003a, b, 2006; Legge et al., 2006; Edelman-Furstenberg et al., 2009; Siccha et al., 2009; Trommer et al., 2010, 2011; Hartman et al., 2020). However, sea level and monsoon effects are pronounced in the southern sector due to its close proximity to the adjacent Arabian Sea (Locke and Thunell, 1988; Fenton et al., 2000; Badawi, 2015). The present study focuses on sediment core FA09 from the Farasan Archipelago (16.93°N, 41.12°E, 302 m water depth) retrieved from the deep outer part of the southern Red Sea continental shelf (Fig. 1b) during the DISPERSE project (Bailey et al., 2015). Geraga et al. (2019) presented initial micropaleontological results for the upper half of the core. Here, we present high-resolution micropaleontological (planktic foraminifera), stable isotope ($\delta^{18}\text{O}$, $\delta^{13}\text{C}$), and transfer-function (Artificial Neural Networks) analyses of paleo-sea surface temperature (SST) and salinity (SSS) on the entire core, spanning the last 30 ka. Our results are integrated with other records from the surrounding area (Fig. 1a, Table 1) to evaluate the regional paleoceanographic evolution. We thus advance our understanding of the spatial variation of Red Sea oceanographic changes over time, and specifically highlight interactions between the southern section and the NWArs since the late Marine Isotope Stage 3.

OCEANOGRAPHIC BACKGROUND

Today, the Red Sea is characterized by arid, subtropical conditions (see Table 2 for data) and is one of the warmest and saltiest

Table 2. Modern annual mean sea-surface temperature and salinity (SST, SSS) values throughout the Red Sea, Gulf of Aden (GoA), and northwestern Arabian Sea (NWARs). Data obtained from the World Ocean Atlas 2018 database (Locarnini et al., 2018; Zweng et al., 2018).

Region	Mean annual SST (°C)	Mean annual SSS (psu)
Southern Red Sea	29.1	38.3
Central Red Sea	27.8	39.4
Northern Red Sea	25.5	40.2
Gulf of Aden (GoA)	25.7	36.0
Northwestern Arabian Sea (NWARs)	25.5	36.1

marine basins in the world (Sofianos and Johns, 2007; Chaidez et al., 2017). The basin's hydrography is largely controlled by the seasonal variations of the SAMS. The SAMS is defined by seasonal movement of the winter-hemisphere Hadley cells across the equator, which also controls the latitudinal position of the Intertropical Convergence Zone (ITCZ) and the extent of the monsoonal rainbelt (Donohoe et al., 2013; McGee et al., 2014).

During the winter season (October–May), the ITCZ approaches 10°S over Asia (Joseph et al., 1994) and NE monsoon (NEM) winds prevail over the Red Sea (Fig. 1a), causing the formation of a two-layered circulation pattern in the Bab el Mandeb straits, which in turn affects the southern sector of the basin. The top layer consists of GoA surface water (GASW) inflow that is characterized by relatively low salinity (~36 psu), high temperature (30°C), and occasionally elevated nutrient contents (Raitso et al., 2015; Sofianos and Johns, 2015; Kürten et al., 2019). Red Sea outflow water (RSOW), which occurs below GASW, is formed in the northern Red Sea and discharges out of the basin as a relatively cold (20–23°C) and highly saline (>40 psu) water mass that is present throughout the year (Woelk and Quadfasel, 1996; Sofianos and Johns, 2015). The NEM winds are remarkably increased when coinciding with prolonged positive (warm) phases of the El Niño–Southern Oscillation (ENSO) Index, facilitating the northward horizontal advection of fertile water masses from GoA into the Red Sea (Raitso et al., 2015; Dasari et al., 2018). In summer (June–September), the ITCZ shifts toward its northernmost position over Asia (Joseph et al., 1994). Resultant southwestern monsoon winds (SWM) cause a three-layered system of water masses in the southern Red Sea (Fig. 1a). SWM winds drive intense upwelling in the NWARs and the GoA, thus increasing productivity levels and decreasing sea-surface temperature and salinity (down to 20°C and 35 psu, respectively) (Anderson and Prell, 1992; McCreary et al., 1996; Gittings et al., 2017). This nutrient-enriched water mass, named Gulf of Aden Intermediate Water (GAIW), enters the southern Red Sea as a subsurface intrusion at 30–60 m water depth and moves northwards to ~24°N before it fully diminishes (Sofianos and Johns, 2007; Churchill et al., 2014; Dreano et al., 2016). Above GAIW, Red Sea Surface Water (RSSW) exits the basin into the GoA. This surface layer has low nutrient concentrations (Li et al., 2018) and high salinity and temperature of 38–40 psu and 28–32°C, respectively (Sofianos and Johns, 2015).

METHODS

Core description and chronology

Core FA09 (total length = 264 cm) was recovered from the outer continental shelf of the southern Red Sea, near the Farasan Archipelago (Figs. 1, 2). Visual core description included down-core grain-size estimates, color, and sedimentary structures (Mazzulo and Graham, 1988). The macroscopic observations led to the identification of different lithological units and were used to guide sampling resolution for the analytical proxies.

Five samples of ~10 mg of *Globigerinoides ruber* (forma alba) specimens from selected intervals were used for ¹⁴C AMS dating at the Scottish Universities Environmental Research Centre (SUERC). The radiocarbon results (Table 3) were calibrated using the Calib v.8.2 software (Stuiver et al., 2022). The Marine20 curve (Heaton et al., 2020) was used and the nearest available ΔR value was selected for reservoir corrections (ΔR: -59 ± 38), obtained from the Marine20 database (Southon et al., 2002; Heaton et al., 2020). Linear sedimentation rates were calculated along the core; however, low-resolution dating provided only rough estimates.

Planktic foraminifera

Planktic foraminiferal assemblages were quantified for 124 samples. The vertical sampling resolution ranged between 1–3 cm. All samples were wet sieved with distilled water, and ultrasonically cleaned to remove coatings. Foraminiferal analyses used aliquots of dried and weighed sediment samples containing >200–300 specimens in the 150–500 μm size fraction. In the sedimentary interval of 130–164 cm, foraminiferal abundances were extremely low, so that examined aliquots had to be limited to only 50 individuals in some cases (Supplementary file 1).

Specimens were counted and identified to species level based on the World Register of Marine Species database taxonomy (WoRMS Editorial Board, 2021). In this study, *Trilobatus sacculifer* includes the *T. trilobus* forma (after Schiebel and Hemleben, 2017). We also grouped *Globigerinella siphonifera* with *G. calida* as *Globigerinella* spp., and *Neogloboquadrina incompta* with *N. dutertrei* as *Neogloboquadrina* spp. Each species was quantified as number of specimens per gram (N/gr) and as percentage of the total planktic foraminifera population (%). In addition, fluxes of planktic foraminifera species were calculated using the relationship:

$$\text{FLUXES} = \text{DBD} \times \text{LSR} \times (\text{N/gr}),$$

where DBD is the dry bulk density of the sediment sample (gr/cm³) and LSR is the linear sedimentation rate (cm/ka). DBD was calculated in each sample following the gravimetric method of McNeill et al. (2019). Fluxes are expressed as N/cm²/ka.

For the purpose of this study, two indices were employed: the Upwelling Index and the Paleoproductivity (PP) curve. The first was calculated as the ratio of the sum of fluxes of the species that prefer rich nutrient conditions related to upwelling (*G. bulloides* and *Neogloboquadrina* spp.; Conan and Brummer, 2000; Schiebel et al., 2004) versus the fluxes of those species that favor oligotrophic conditions (*Gs. ruber* and *T. sacculifer*; Conan and Brummer, 2000; Schiebel et al., 2004). The PP curve was determined as the sum of *G. glutinata*, *G. bulloides*, *B. digitata*, *T. quinqueloba*, and *Neogloboquadrina* spp. expressed as percentages. These species are associated with high-productivity

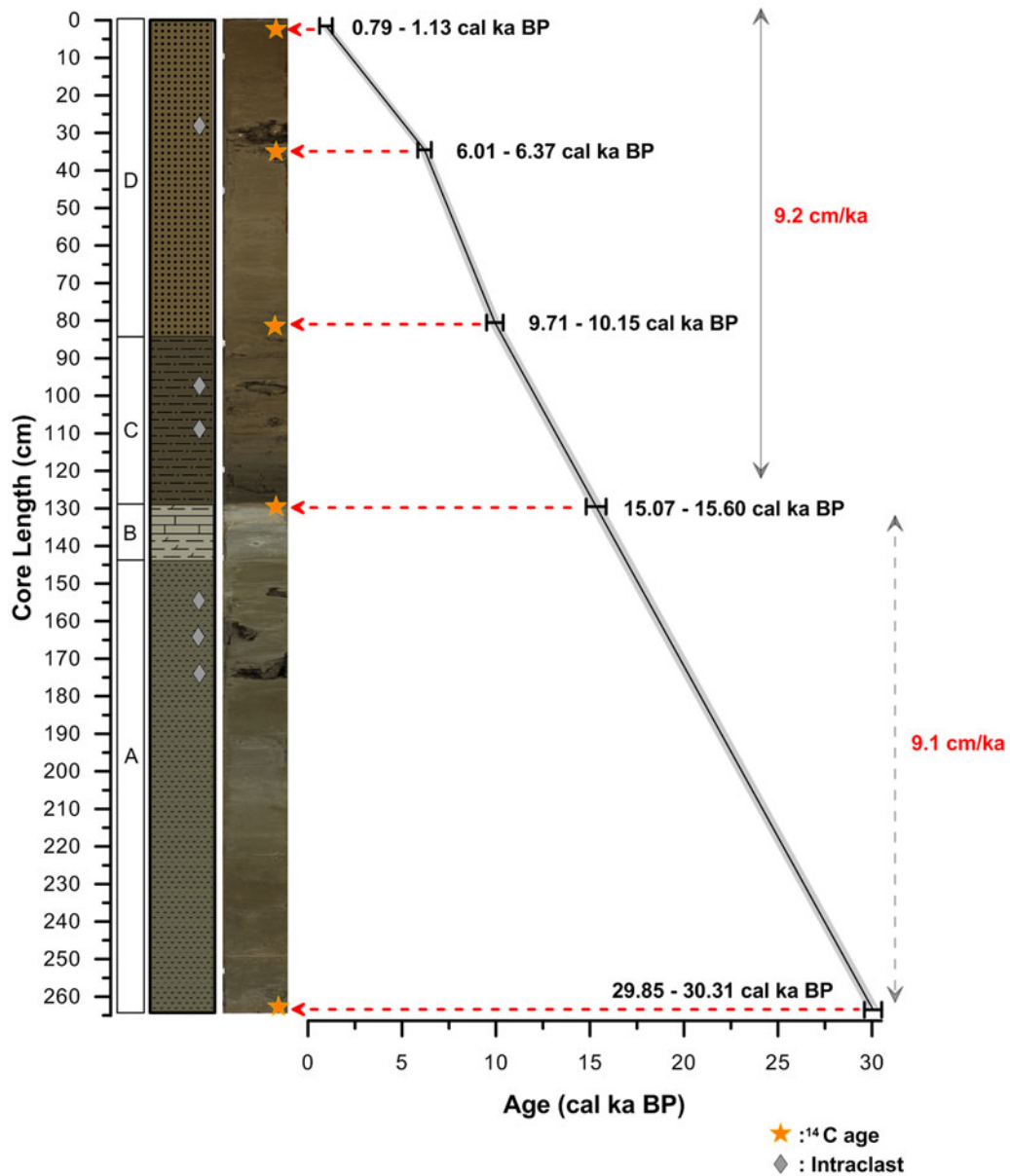


Figure 2. Lithological intervals (A–D), stratigraphic column, and core photo of FA09, followed by the calibrated ages (2σ). The age/depth association is based on linear interpolation between the age points. Mean linear sedimentation rates for the glacial (low resolution) and interglacial sections are also shown.

conditions and increased phytoplankton concentrations (Be and Tolderlund, 1971; Pujol and Vergnaud-Grazzini, 1995; Schiebel and Hemleben, 2017). Neither of the above indices was valid between 130–164 cm due to the severe drop of the planktic foraminifera population.

Multivariate statistical analysis with varimax rotation (R-mode factor analysis; Reyment and Joreskog, 1996) was performed on the foraminiferal dataset using the statistical software SPSS v25 to investigate downcore associations that can be related to paleo-environmental changes. The statistical treatment was performed for both fluxes (N/cm²/ka) and relative abundance (%) foraminiferal datasets (Supplementary file 3). The final number of selected factors, based on statistical criteria suggested by Reyment and Joreskog (1996), mainly concerned the amount of total variance explained on the dataset and communality values of the variables. Variables that displayed a rotated loading >0.5 were considered

significantly loaded on a factor (Hair et al., 2006). The downcore variation of the extracted factor scores was calculated by summing the products of factor loadings and the corresponding original data (Papatheodorou et al., 2006).

Stable isotopes

Oxygen ($\delta^{18}\text{O}$) and carbon ($\delta^{13}\text{C}$) isotope ratios were measured for 105 samples. For each sample, 20–30 specimens of *Gs. ruber* (forma alba) were hand-picked, crushed, and ultrasonically cleaned with ethanol. Measurements were conducted at the Research School of Earth Sciences at Australian National University using a Thermo Fisher Scientific Delta Advantage mass spectrometer coupled to a Kiel IV microcarbonate preparation device. Isotope data were normalized to the Vienna Pee Dee Belemnite (VPDB) scale using NBS-19 and NBS-18 carbonate

Table 3. Radiocarbon and calibrated ages for the FA09 core, including 2 σ range and uncertainties.

Sample Reference	Sample depth(cm)	Radiocarbon Age (yrs BP)	Calibrated Age Range (2 σ) (cal ka BP)	Mean Calibrated Age (cal ka BP)
FA09 – Sample 1	1.5	1515 \pm 32	0.79–1.13	0.96 \pm 0.17
FA09 – Sample 2	34.5	5916 \pm 32	6.01–6.37	6.20 \pm 0.18
FA09 – Sample 3	80.5	9252 \pm 32	9.71–10.15	9.94 \pm 0.22
FA09 – Sample 4	129.5	13366 \pm 56	15.07–15.60	15.33 \pm 0.27
FA09 – Sample 5	263.5	26655 \pm 86	29.85–30.31	30.06 \pm 0.23

standards. The external reproducibility (1 σ) of an in-house carbonate standard (N = 8) and NBS-19 (N = 23) was better than $\pm 0.06\%$ for $\delta^{18}\text{O}$ and $\pm 0.03\%$ for $\delta^{13}\text{C}$.

Sampling and measurement resolution between 130–164 cm was reduced to only four samples because of a severe reduction in *Gs. ruber* specimens. Therefore, the isotope-related interpretation within this interval is limited to a more general perspective.

Paleotemperature (SST_{ANN}) and paleosalinity (SSS_{ANN})

Sea surface temperature (SST, $^{\circ}\text{C}$) and sea surface salinity (SSS) were reconstructed on the basis of Artificial Neural Network (ANN) simulations. ANNs are computing systems that consist of highly interconnected sets of information-processing units (neurons) similar to biological neurons (Sarkar and Pandey, 2015) that have the ability to overcome problems of non-linear relationships between the input and output variables (Naidu and Malmgren, 2005).

The principal concept of the ANN function is reproduction of output variable(s) from certain input variables through a specific training process (Malmgren and Nordlund, 1997). In the present study, ANNs were trained on a dataset of planktic foraminiferal percentage associations from surrounding core-top samples of sites with given SST and SSS values (calibration dataset) and then employed on the downcore planktic foraminiferal percentages of FA09 (downcore dataset). The calibration dataset contained a total of 758 sites covering the Red Sea (Auras-Schudnagies et al., 1989; Siccha et al., 2009), the Indian Ocean (Barrows and Juggins, 2005; Munz et al., 2015), and the Mediterranean Sea (Hayes et al., 2005) (Supplementary file 2, Figure SF2_1, Table SF2_1). Associated modern SST and SSS values (annual mean) were obtained from the World Ocean Atlas 2018 database (Locarnini et al., 2018; Zweng et al., 2018).

Reliability of the ANN results in the Red Sea, where a specific oceanographic regime prevails in comparison to the open ocean, is founded on the degree of analogy between the calibration and downcore datasets (Siccha et al., 2009; Trommer et al., 2010). In the present study, both datasets are represented by 23 variables; each one standing for a particular planktic species or group (Supplementary file 2, table SF2_2). The mean value of each variable in the calibration dataset was quite similar to the corresponding variable in the downcore dataset, leading to a very strong correlation between the two ($R^2 = 0.897$), and therefore an efficient analogy is inferred (Supplementary file 2, Table SF2_2, Figure SF2_2). However we need to clarify that our simulations are based on annual SST and SSS average values along with numbers of planktic percentage associations, and as such, our results do not take seasonality into consideration. For this reason, our SST and SSS estimates should be treated with caution, focusing more on the trend pattern rather than on the

absolute values. In addition, all the interpretations regarding paleotemperature and paleosalinity are always combined and compared with the faunal and isotopic data of FA09 in order to increase the validity of the ANN results.

The ANN simulations were performed using Matlab. For the ANN training procedure, the dataset was subdivided into two random portions: the training set, which was used for training the ANN; and the test set, to which the trained network was applied (Demuth et al., 2007). The training set consisted of 606 samples (80%) and the test set of the remaining 152 samples (20%). Evaluation of the simulations was based on performance indices for their test set. The Root Mean Square Error (RMSE) and correlation coefficient (R) were calculated and served as performance indices (Siccha et al., 2009). The final exported networks displayed a RMSE = 0.987, R = 0.93 for SST, and RMSE = 0.464, R = 0.95, for the SSS distribution, suggesting a highly reliable degree of prediction for both parameters (Liu and Chen, 2012; Gebler et al., 2020). Further details on the ANN methodology can be found in Hadjisolomou et al. (2016) and references therein.

Data incorporation and terminology

Our data were compared with other records from the surrounding area (see Table 1 for list of records) for more robust interpretations. The chronological framework of cores #10, 13, and 15 was re-calculated with the Calib v.8.2 software (Stuiver et al., 2022), applying the Marine20 curve and ΔR : 49 ± 57 (Southon et al., 2002; Heaton et al., 2020; see Supplementary file 4). All isotopic ($\delta^{18}\text{O}$, $\delta^{13}\text{C}$) records presented in this study have been performed on the same carbonate material (*Gs. ruber* forma alba tests), thus leading to highly reliable comparisons. Additionally, we correlated our findings with the northern Hemisphere summer insolation index (65°N), after Laskar et al. (2004), and the sea level variation of the last 30 ka. More particularly for sea level, we used the Red Sea-based curves of Grant et al. (2012) and Arz et al. (2007) for the 30–7 ka interval, integrated with available radiometrically dated sea level markers (coral and reef terraces, beachrocks, shell middens, etc.) distributed along the Red Sea coastal borders spanning the last 7 ka. These markers were synthesized and presented in the study of Al-Mikhlaifi et al. (2021).

Concerning (chrono)stratigraphic terms, we refer to the 30–15 ka period as the glacial time interval of the studied core, which covers the end of Marine Isotope Stage 3 and Marine Isotope Stage 2. Subsequently, the last 15 ka are regarded as the interglacial interval, which includes the deglacial sea level rise (Cronin, 2012). The interglacial interval is divided in the late glacial (ca. 15–11 ka) and the Holocene (last 11 ka) intervals. The latter is further divided into Early (ca. 11–8 ka), Middle (ca. 8–4 ka), and Late (last 4 ka) Holocene, according to

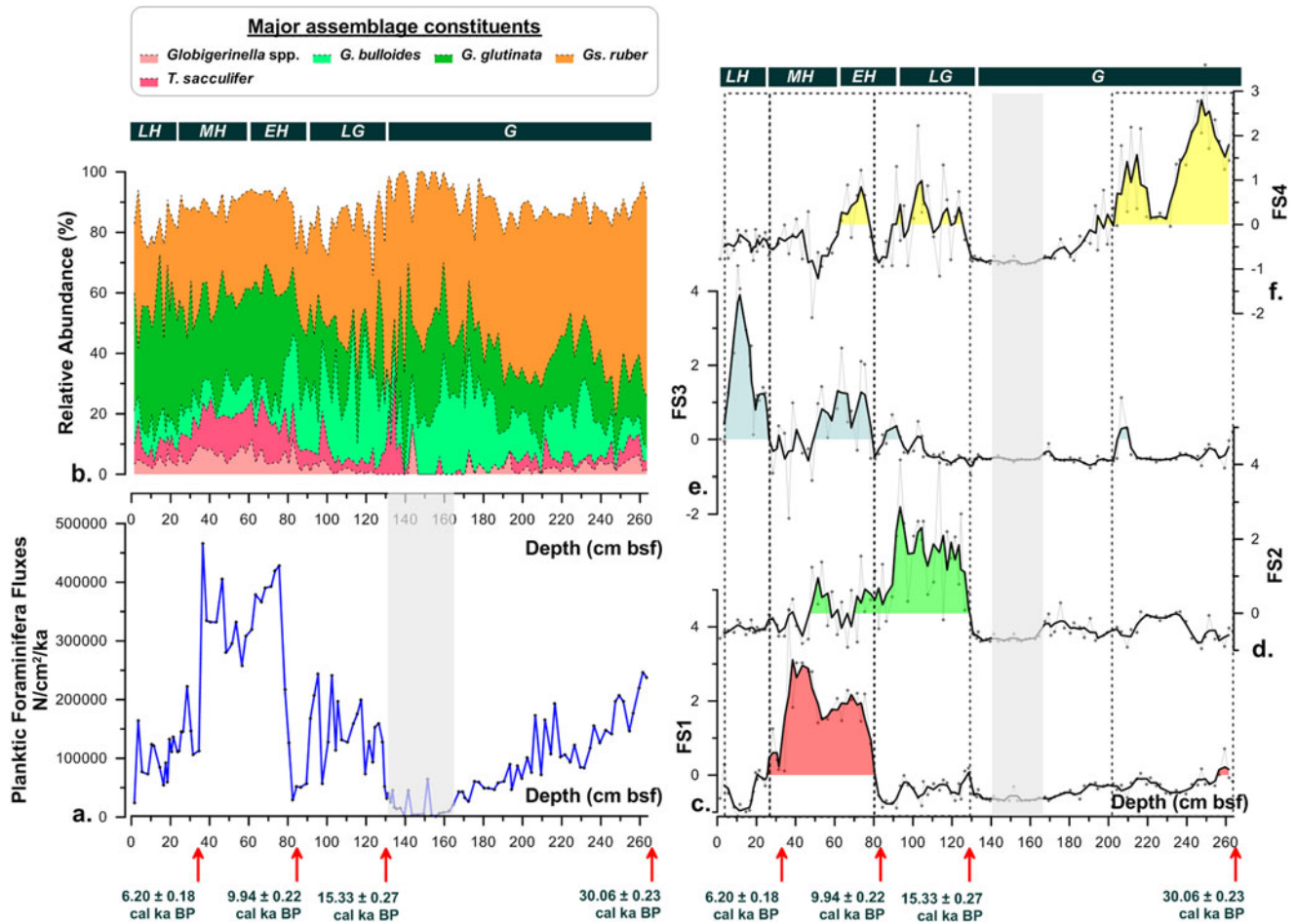


Figure 3 (a) Total planktic foraminiferal fluxes shown as N/cm²/ka. (b) Relative abundance of the major assemblages. (c–f) Factor scores (FS) 1–4, in core FA09. The sections of increased FS values are indicated with dashed rectangles. The interval of severe drop in planktic foraminiferal assemblages (130–164 cm) is marked in light gray color. The top horizontal bars represent glacial (G), late glacial (LG), Early Holocene (EH), Middle Holocene (MH), and Late Holocene (LH) chronostratigraphic intervals; bsf = below sea floor.

Walker et al. (2012). The boundaries of the above intervals in the FA09 core were approached in an approximate basis, assuming linear sedimentation rates between calibrated radiocarbon dates.

RESULTS

Sediment properties and age control

Core FA09 comprises fine-grained shelf sediments in various brownish color shades, marked by sparse presence of lithic and coral clasts (Fig. 2). The sedimentary succession is divided into four lithological units. The lower unit (Unit A, 264–144 cm) consists of light brownish gray (2.5Y 6/2), fairly homogenous sandy silt. Unit B (144–129 cm), which includes the most prominent lithological feature, incorporates light gray (2.5Y 7/1) to white (2.5Y 8/1), highly condensed sandy silt, marked by an abrupt contact with the overlying sediments. Unit C (129–84 cm) displays a notably different pattern and consists of weakly laminated, very dark grayish brown (2.5Y 3/2) to olive brown (2.5Y 4/3) silt. The upper unit (Unit D, 84–0 cm) comprises light olive brown (2.5Y 5/4) sandy silt with an upward coarsening trend.

The chronological framework of core FA09 is based on calibrated radiocarbon ages, which show an overall 2σ uncertainty of ± 0.2 ka (Table 3). The bottom of the core dates to $30.06 \pm$

0.23 cal ka BP, so that the studied sedimentary succession spans a time period from the final phase of Marine Isotope Stage 3 to the present. Linear sedimentation rate suggests an average value of 9.2 cm/ka for the last ca. 15 ka, while a mean value of 9.1 cm/ka is roughly estimated for the glacial interval (Fig. 2).

Planktic foraminiferal assemblages

Planktic foraminifera are present throughout the FA09 core. Their fluxes display considerable variability (Fig. 3a), reaching lowest values between 130–164 cm (~ 1400 N/cm²/ka) and highest values between 36–75 cm (up to 355,200 N/cm²/ka).

Globigerinoides ruber is the dominant species in FA09, with a downcore average of 40% of the total population. Other species with substantial presence are *Globigerinella glutinata* (24%), *Globigerina bulloides* (15%), *Trilobatus sacculifer* (6%), and *Globigerinella* spp. (3%). At 88% of the total population, these species form the major assemblage components (Fig. 3b). Other species found in low abundance (<2.5% each) include *Beella digitata*, *Globobulimina rubescens*, *Globigerinoides tenellus*, *Globigerinoides conglobatus*, *Orbulina universa*, *Globobulimina menardii*, *Neoglobobulimina* spp., *Globigerina falconensis*, *Turborotalita quinqueloba*, and *Hastigerina pelagica*. Counts,

Table 4. Communalities and varimax rotated factor loadings (R-mode) of the planktic foraminiferal fluxes dataset. Variables with loadings ≥ 0.5 are highlighted in bold.

Variable	Communalities	Rotated Component Matrix			
		Factor 1	Factor 2	Factor 3	Factor 4
<i>Globigerinoides ruber</i>	0.852	0.674	0.140	0.075	0.610
<i>Trilobatus sacculifer</i>	0.900	0.923	0.098	0.189	0.051
<i>Hastigerina pelagica</i>	0.548	0.410	0.066	0.611	-0.047
<i>Globigerinella</i> spp.	0.814	0.885	-0.005	0.162	0.067
<i>Globigerinita glutinata</i>	0.821	0.822	0.106	0.336	0.145
<i>Neogloboquadrina</i> spp.	0.633	0.505	0.600	0.087	-0.100
<i>Globigerina bulloides</i>	0.831	0.324	0.838	-0.047	0.147
<i>Globigerinoides tenellus</i>	0.581	0.737	0.013	-0.140	-0.137
<i>Globoturborotalita rubescens</i>	0.525	0.679	0.119	0.205	0.089
<i>Beella digitata</i>	0.818	-0.108	0.897	0.036	-0.014
<i>Globorotalia menardii</i>	0.809	-0.198	0.571	-0.138	0.651
<i>Turborotalita quinqueloba</i>	0.745	-0.052	-0.011	0.861	-0.022
<i>Globigerinoides conglobatus</i>	0.832	0.110	-0.075	-0.168	0.886
<i>Orbulina universa</i>	0.610	0.234	-0.036	0.723	-0.177
Explained Variance (%)		31.6	16.1	13.9	12.2

percentages, and fluxes for all species are presented in Supplementary file 1.

The R-mode factor analysis showed good agreement between fluxes and relative abundance data, resulting in rather similar factors (Supplementary file 3). Nevertheless, because multivariate analysis is more effective on statistically independent variables (Reyment and Joreskog, 1996; Kite and Whitley, 2018), we choose to focus on the fluxes data. A four (4) factor model was utilized to describe the planktic foraminiferal associations. These factors explain 74% of the total variance, and each variable shows communalities higher than 0.5 (Table 4). This means that the 4-factor model sufficiently expresses the analyzed variables (Reyment and Joreskog, 1996). The downcore variation of each factor score (FS1–FS4) is presented in Figure 3c–f. Note that none of the extracted factors describes the 130–164 cm interval due to the severe reduction in planktic foraminiferal fluxes.

The four factors are presented in Table 4. The first factor (Factor 1) explains the largest proportion (32%) of the total variance and displays high positive loadings for *Gs. ruber*, *T. sacculifer*, *G. glutinata*, *G. rubescens*, *Gs. tenellus*, *Globigerinella* spp., and *Neogloboquadrina* spp. All these species occur in the living planktic associations and in Holocene assemblages in the southern Red Sea (Locke and Thunell, 1988; Auras-Schudnagies *et al.*, 1989; Siccha *et al.*, 2009). The highest FS1 values are recorded between 28–80 cm (Fig. 3c), covering the largest part of Early and Middle Holocene. The second factor (Factor 2) explains a significant proportion (16%) of the total variance and shows high positive loadings for *G. bulloides*, *Neogloboquadrina* spp., *G. menardii*, and *B. digitata*. The highest FS2 values are observed at 80–129 cm, corresponding to the late glacial interval; yet they remain at an increased level up to 50 cm (Fig. 3d), which suggests an important contribution until mid-Holocene. Factor 3 explains 14% of the total variance and displays high positive loadings for *T. quinqueloba*, *Or. universa*,

and *H. pelagica*, while the highest FS3 values are recorded at the top 28 cm (Fig. 3e), implying a dominance during Late Holocene. Notable increases are also observed between 50–80 cm and ~200–210 cm. The final factor (Factor 4) explains 12% of the total variance and exhibits high positive loadings for *Gs. conglobatus*, *Gs. ruber*, and *G. menardii* (Fig. 3f). The highest FS4 values are recorded at the lowermost 60 cm of the core (with an interruption at ~220–227 cm), covering the lower half of the glacial interval. Oscillations between high and low FS4 values were also recorded during the late glacial and Early Holocene (60–129 cm). Detailed information on the ecological interpretation of each factor is presented in Supplementary file 5.

The Upwelling Index and PP curve (Figs. 5e, 7b) show high similarity and display the highest values during the late glacial (80–129 cm), while they also are increased at 165–185 cm and 215–235 cm, suggesting temporal enhancement during the glacial interval as well. However, a notable rise of the PP curve is observed at 5–25 cm, which is <5 ka old and not followed by increased Upwelling Index values.

In addition, we note that the decrease in the paleoproductivity curve between 34–68 cm (Fig. 7b) acts as a side effect of the much-increased FS1 values and the high abundance of *Gs. ruber*, *T. sacculifer*, and *Globigerinella* spp. In fact, the absolute numbers of productivity-related species point to a rather fertile environment for that interval (Supplementary file 1).

Stable isotopes

The $\delta^{18}\text{O}$ record of FA09 (Fig. 4a) ranges between -2.4‰ and 2.1‰ and displays more positive values (mean 1.1‰) in the glacial section, and is followed by intermediate values for the late glacial and lighter values in the Holocene sediments (mean -1.9‰). Moreover, FA09 contains a negative $\delta^{18}\text{O}$ anomaly at

165–185 cm, and two sharp positive $\delta^{18}\text{O}$ anomalies at ~ 84 cm and 97 cm.

The $\delta^{13}\text{C}$ record of FA09 ranges between -0.6 and 1.7‰ (Fig. 4b). A gradual decreasing trend is noted in the glacial section of the core, from $\sim 1\text{‰}$ at the base to nearly -0.25‰ around 130 cm (ca. 15 ka). The lowest values are observed within the late glacial interval. This trend reverses afterwards, leading to a prominent $\delta^{13}\text{C}$ increase at around the Holocene transition. The $\delta^{13}\text{C}$ values remain high throughout the Holocene interval, with mean values of $\sim 1.2\text{‰}$.

Paleotemperature (SST_{ANN}) and paleosalinity (SSS_{ANN})

Reconstructed SST_{ANN} and SSS_{ANN} records vary between $22\text{--}30^\circ\text{C}$ and $34.3\text{--}39.3$ psu, respectively (Fig. 4c, d). Two intervals of notable temperature-salinity associations are distinguished: one within the glacial interval (130–190 cm) and another one that covers most of the Holocene deposits (upper 80 cm). The former corresponds to the lowest SST (mean 23.7°C) and highest SSS (mean 37.8 psu) trends, while the later coincides with both increased SST and SSS levels, with mean values of 28.2°C and 37.5 psu, respectively. Notably, for most of the Holocene interval, both SST_{ANN} and SSS_{ANN} fluctuate close to present day mean values (Fig. 4c, d; Table 2). The lowest SSS_{ANN} levels are observed at the lower half of the glacial interval (190–264 cm) and during the late glacial interval (80–129 cm), with mean values of ~ 36 psu.

We need to note here that because planktic foraminifera-based SSS_{ANN} reconstructions have been considered as misleading in the literature (Wolff et al., 1999, and references therein), and despite the efficiency in our ANN simulations, the salinity results are closely compared with records from the surrounding area and are assessed in close conjunction with the isotopic and faunal data of the core in the present study for more robust interpretations.

DISCUSSION

Our results combined with previous findings from the surrounding area address two major subjects. The first regards the regional oceanographic differences in terms of glacial-interglacial shifting, while the second deals with arguments on the relationship between environmental conditions and monsoon variability over the last 30 ka. However, we are aware of the weakness derived from the low-resolution dating of the studied core and, consequently, observations and interpretations on short timescales are diminishing in importance. The FA09 records are discussed in terms of downcore variations (depth-wise), while chronological control is provided by correlation with other regional, dated records in conjunction with the calibrated radiocarbon dates of the studied core (Figs. 5–7).

Glacial-interglacial shift in the southern Red Sea records: the essential influence of sea level changes, solar intensity, and ITCZ progression in the Arabian-Red Sea water-exchange pattern

Observing the downcore variation of the FA09 records, we detect two synchronized, sharp shifts where strong coupling occurs—at the boundaries of lithological units B-C and C-D (Figs. 2, 5, 6). The lower coincides with onset of the late glacial interval, dated at ca. 15 ka, and is principally represented by a notable rise of SST_{ANN} and planktic foraminiferal numbers, and a drop of

SSS_{ANN} $\delta^{18}\text{O}$ and $\delta^{13}\text{C}$ values (Figs. 5c–f, 6). The upper one dates to ca. 10 ka and is characterized by a concurrent rise of SST_{ANN} , SSS_{ANN} , and $\delta^{13}\text{C}$, with parallel reduction of $\delta^{18}\text{O}$ and Upwelling Index (Figs. 5c–f, 6). The combination of the later shift reflects the development of warm, saline, and nutrient-rich surface waters, and refers to the dominance of a well-stratified, three-layered water circulation mode with the RSSW overlying the GAIW intrusion. Our suggestion is in close agreement with the findings of Siddall et al. (2002), who suggested an age of ca. 10.5 ka for the onset of the GAIW intrusion through the straits of Bab el Mandeb.

The above observations imply that the transition from glacial to late glacial and Holocene intervals was accompanied by pronounced hydrological modifications in the southern Red Sea. In order to examine the mechanisms behind these modifications, we thoroughly discuss the variation of the examined records in FA09 (isotopic, SST, SSS) together with similar records of sediment cores from the surrounding area (Figs. 5, 6). In this way we aim to (1) evaluate the paleoceanographic history of the southern Red Sea in a glacial-interglacial basis, (2) identify the triggering forces responsible for hydrological conversions, and (3) provide further knowledge on the overall Arabian-Red Sea interaction for the last 30 ka.

The $\delta^{18}\text{O}$ record

Comparison between the southern Red Sea $\delta^{18}\text{O}$ record (core FA09) and those of NWARs (cores #10, 11, 13, 15), GoA (cores #8, 9), central (core #4), and northern (cores #6, 7) Red Sea reveals generally similar patterns for the last 30 ka (Fig. 5c). However, the absolute values among the records are different. The $\delta^{18}\text{O}$ record of FA09 displays a glacial-interglacial amplitude of only 3‰ , compared with $5\text{--}6\text{‰}$ in the central and northern Red Sea. This gradient has been attributed to predominance of the marginal-basin concentration effect during glacial times in the central to northern sectors, and greater effect of GoA inflow in the southern sector (Siddall et al., 2004). During the glacial period, the $\delta^{18}\text{O}$ is $1\text{--}2\text{‰}$ more positive in the southern Red Sea than in the GoA and NWARs, but more negative than in the central and northern parts of the Red Sea basin. The most significant difference among the records is observed around the MIS2 sea level lowstand (ca. 22–15 ka) (Fig. 5a, c). Subsequently, the $\delta^{18}\text{O}$ differences among the five regions become smaller, thus implying ongoing water exchange between the seas. All these observations parallel the sea level fluctuations for the last 30 ka (Fig. 5a), supporting the findings of Siddall et al. (2003, 2004), who suggested that sea level change is the dominant driver of Red Sea $\delta^{18}\text{O}$ variability.

The minimum differences in the $\delta^{18}\text{O}$ values were observed during the Early Holocene, suggesting efficient water-mass exchange among the five regions (Fig. 5c). In addition, it is most likely that these regions experienced similar precipitation levels at that time, thus leading to similar $\delta^{18}\text{O}$ values. Indeed, during the Early Holocene, insolation intensity reached its peak in the Northern Hemisphere (Fig. 5b), causing a prominent northward migration of the summer ITCZ, thus forming a zone of particularly increased humidity, which included the Arabian Sea (Overpeck et al., 1996; Fleitmann et al., 2007; Munz et al., 2017) and the entire Red Sea basin (Locke and Thunell, 1988; Arz et al., 2003a; Legge et al., 2006). However, after 7 ka, the $\delta^{18}\text{O}$ values are considerably heavier in the northern Red Sea compared to the other regions, according to the gradual decrease of the solar insolation intensity and the southward migration of

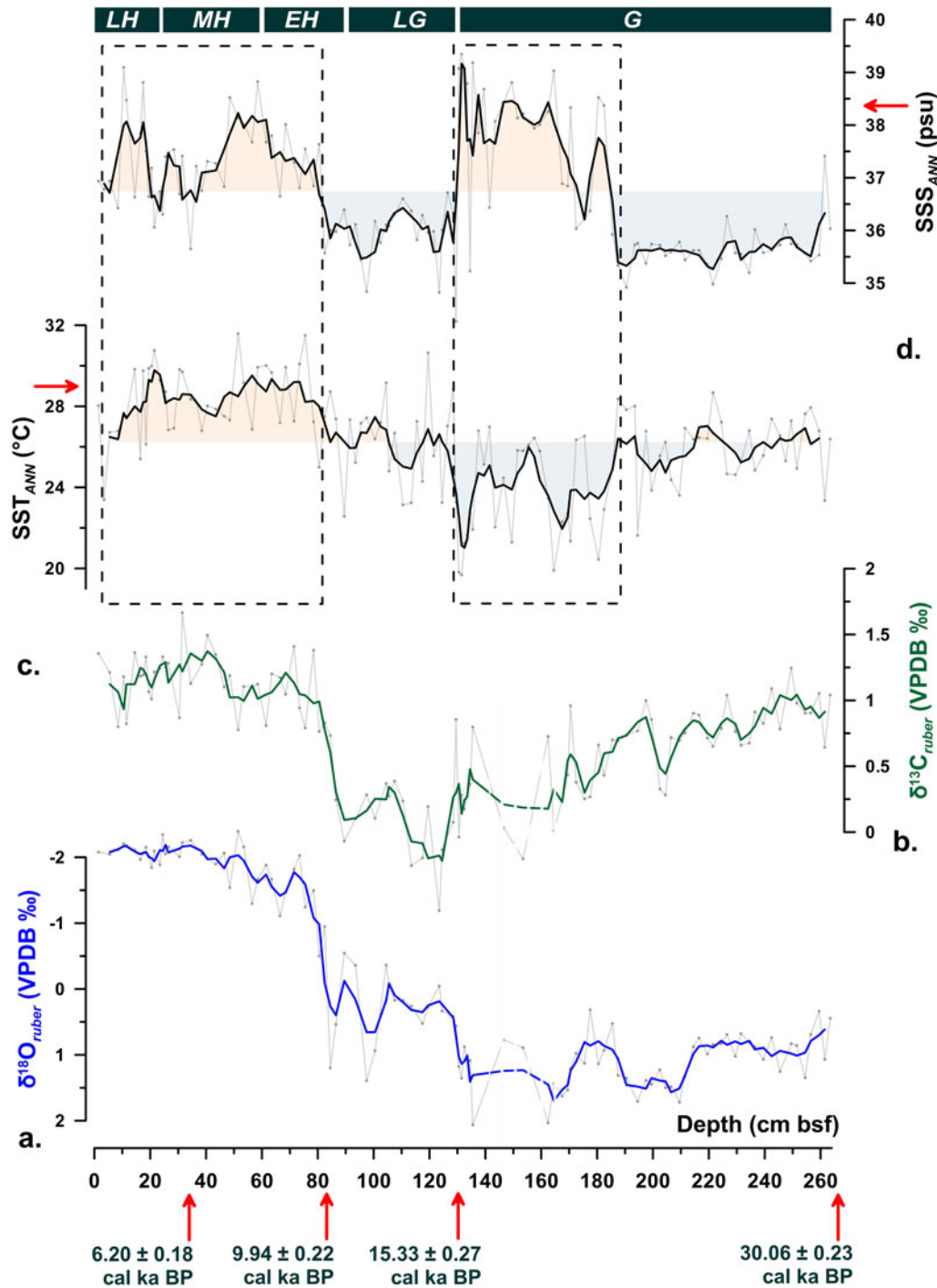


Figure 4 (a) The $\delta^{18}\text{O}_{\text{ruber}}$ and (b) $\delta^{13}\text{C}_{\text{ruber}}$ records of FA09. Blue and green lines represent the 3p running average of each record, respectively. Records appear as dashed lines in the low-resolution interval (130–164 cm). (c) SST and (d) SSS variation of FA09 based on ANN simulations. The upper 80 cm and the 130–190 cm intervals are noted (dashed-line rectangles) according to the text. Modern mean annual SST and SSS values in the southern Red Sea are indicated by horizontal arrows. The top horizontal bars represent glacial (G), late glacial (LG), Early Holocene (EH), Middle Holocene (MH), and Late Holocene (LH) chronostratigraphic intervals; bsf = below sea floor.

the mean ITCZ position (Wang *et al.*, 2005; Fleitmann *et al.*, 2007; Banerji *et al.*, 2020). Fleitmann *et al.* (2007) found that after 6.5 ka, the location of the summer ITCZ and the monsoonal rainbelt was between 23–17°N, thus affecting areas up to south-central parts of the Red Sea, but not the northern sector of the basin. Therefore, aridity and high evaporation must have contributed

to the heavier $\delta^{18}\text{O}$ values in the surface waters of the northern Red Sea (Arz *et al.*, 2003a).

The $\delta^{13}\text{C}$ record

In contrast to $\delta^{18}\text{O}$, the $\delta^{13}\text{C}$ values of core FA09 are heavier in the Holocene (Fig. 5d). The lowest values occur during the late

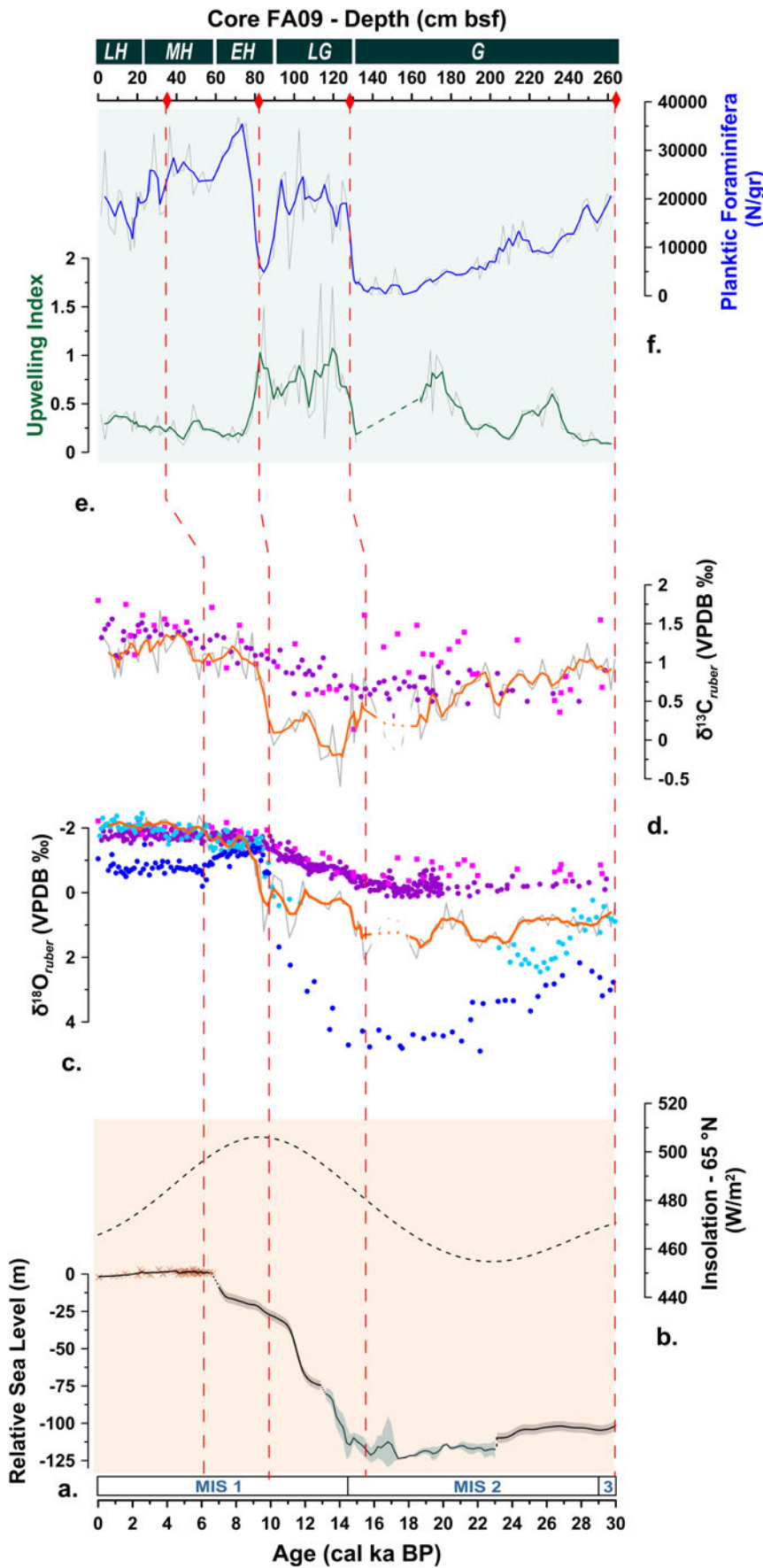


Figure 5 (a) Synthesized relative sea level reconstruction after combining the curves of Grant et al. (2012) (gray-shaded bands) with Arz et al. (2007) (23–13 ka; green-shaded bands) and the coastal sea level markers of Al-Mikhlafla et al. (2021) for the last 7 ka. (b) Northern Hemisphere summer insolation (Laskar et al., 2004). (c) Compilation of the $\delta^{18}O_{ruber}$ record of FA09 (orange line; 3p running average) with records from northwestern Arabian Sea (purple circles; cores #10, 11, 13, 15), Gulf of Aden (magenta squares; cores #8, 9), central Red Sea (light blue circles; core #4), and northern Red Sea (dark blue circles; cores #6, 7). (d) Compilation of the $\delta^{13}C_{ruber}$ record of FA09 (orange line; 3p running average) with records from the northwestern Arabian Sea (purple circles; cores #10, 15) and the Gulf of Aden (magenta squares; cores #8, 9). (e) Upwelling Index in FA09. (f) Total planktic foraminiferal numbers (N/gr) in FA09. Calibrated radiocarbon dates in FA09 are highlighted in red diamond symbols. The FA09 records are always plotted against depth (top x axis). For (c) and (d), see Figure 1 for core locations and Table 1 for data references. The low foraminiferal interval in FA09 (130–164 cm) is dashed in (c–e). Marine Isotope Stages 1–3 from Lisiecki and Raymo, (2005). The top horizontal bars represent glacial (G), late glacial (LG), Early Holocene (EH), Middle Holocene (MH), and Late Holocene (LH) chronostratigraphic intervals; bsf = below sea floor.

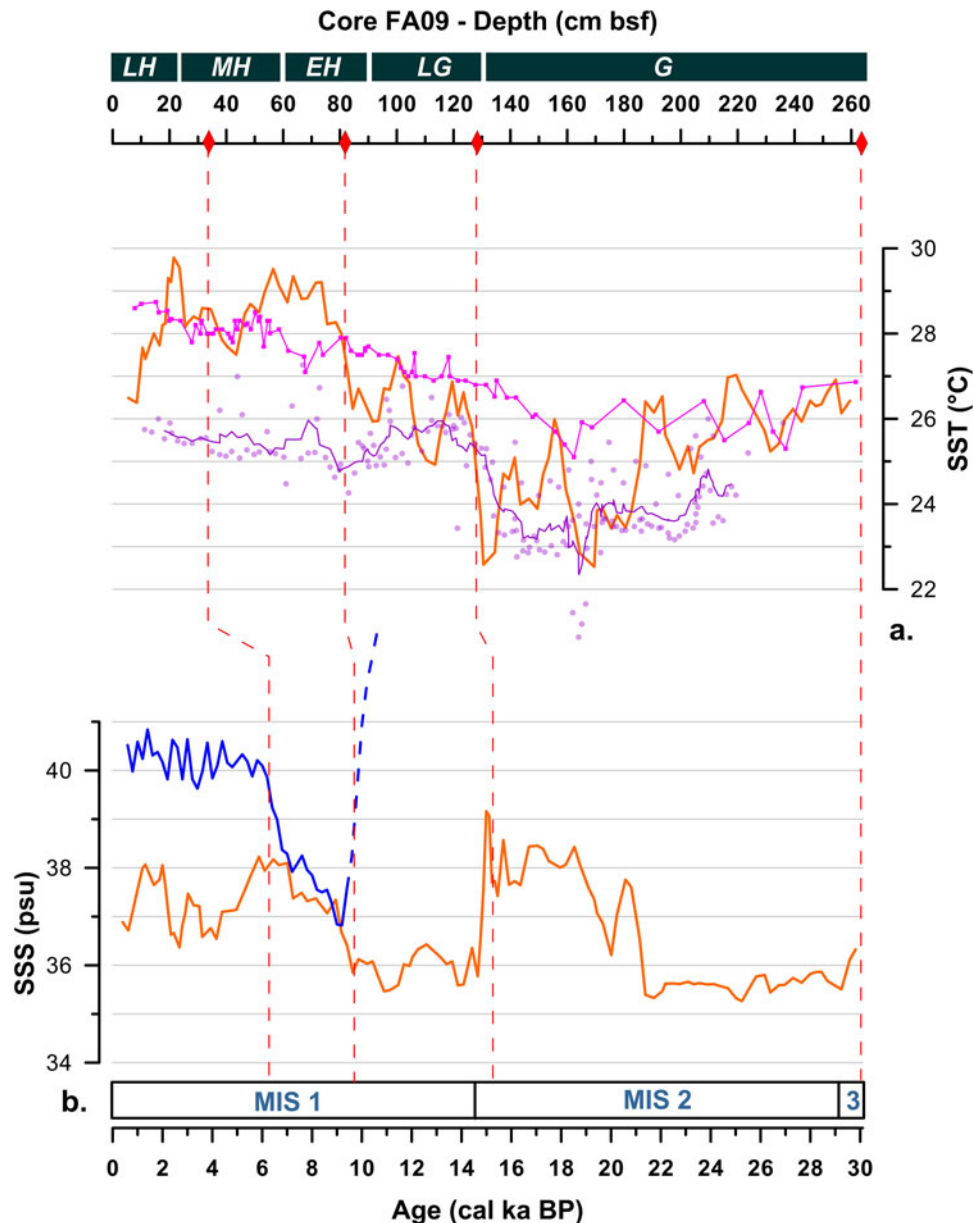


Figure 6 (a) SST variation of FA09 (orange line) along with records from the northwestern Arabian Sea (purple line, 5p running average of combined data from cores #11, 12, 14) and Gulf of Aden (magenta line, core #8). (b) SSS variation of FA09 (orange line) together with data from the northern Red Sea (blue line, core #6). The FA09 data are presented depth-wise (top x axis). The glacial interval of northern Red Sea salinity is not shown due to the largely increased values. For core locations and data references, see Figure 1 and Table 1, respectively. The top horizontal bars represent glacial (G), late glacial (LG), Early Holocene (EH), Middle Holocene (MH), and Late Holocene (LH) chronostratigraphic intervals; bsf = below sea floor.

glacial interval and could be the outcome of increased precipitation and freshwater input levels, reinforced by the intensified insolation (Laskar *et al.*, 2004) and/or the enhanced upwelling of nutrient-rich waters in the euphotic zone (Fig. 5b, e). The former conditions induce the entering of light $\delta^{13}\text{C}$ terrestrial carbon in the seawater, while the latter conditions favor a ^{12}C increase in the mixed layer, which would lead to $\delta^{13}\text{C}$ -depleted surface waters (Rohling and Cooke, 1999; Mackensen and Schmiedl, 2019). Therefore, both conditions could lead to $\delta^{13}\text{C}$ -depleted surface waters. The above likely indicates that the carbon isotopic signal of seawater in our study area is primarily affected by factors such as productivity and water mixing (Rohling and Cooke, 1999). In that sense, the heavy $\delta^{13}\text{C}$ values along with the low

Upwelling Index (Fig. 5e) during the Holocene imply the establishment of well-stratified water column conditions in the southern Red Sea.

Comparison of the FA09 $\delta^{13}\text{C}$ record with similar records from NWArs (cores #10, 15) and the GoA (cores #8, 9) (Fig. 5d) uncovered relatively common Holocene values, reflecting the efficient interaction of these areas after the deglacial sea level rise. However, the southern Red Sea presents a notable offset from the NWArs and GoA records for the upper part of the glacial interval (~130–180 cm in FA09) and during the late glacial. Concerning the former interval, this offset coincides with major reduction of the planktic faunal population, which peaked between 130–164 cm in FA09 (Fig. 5d, f). Although chronological

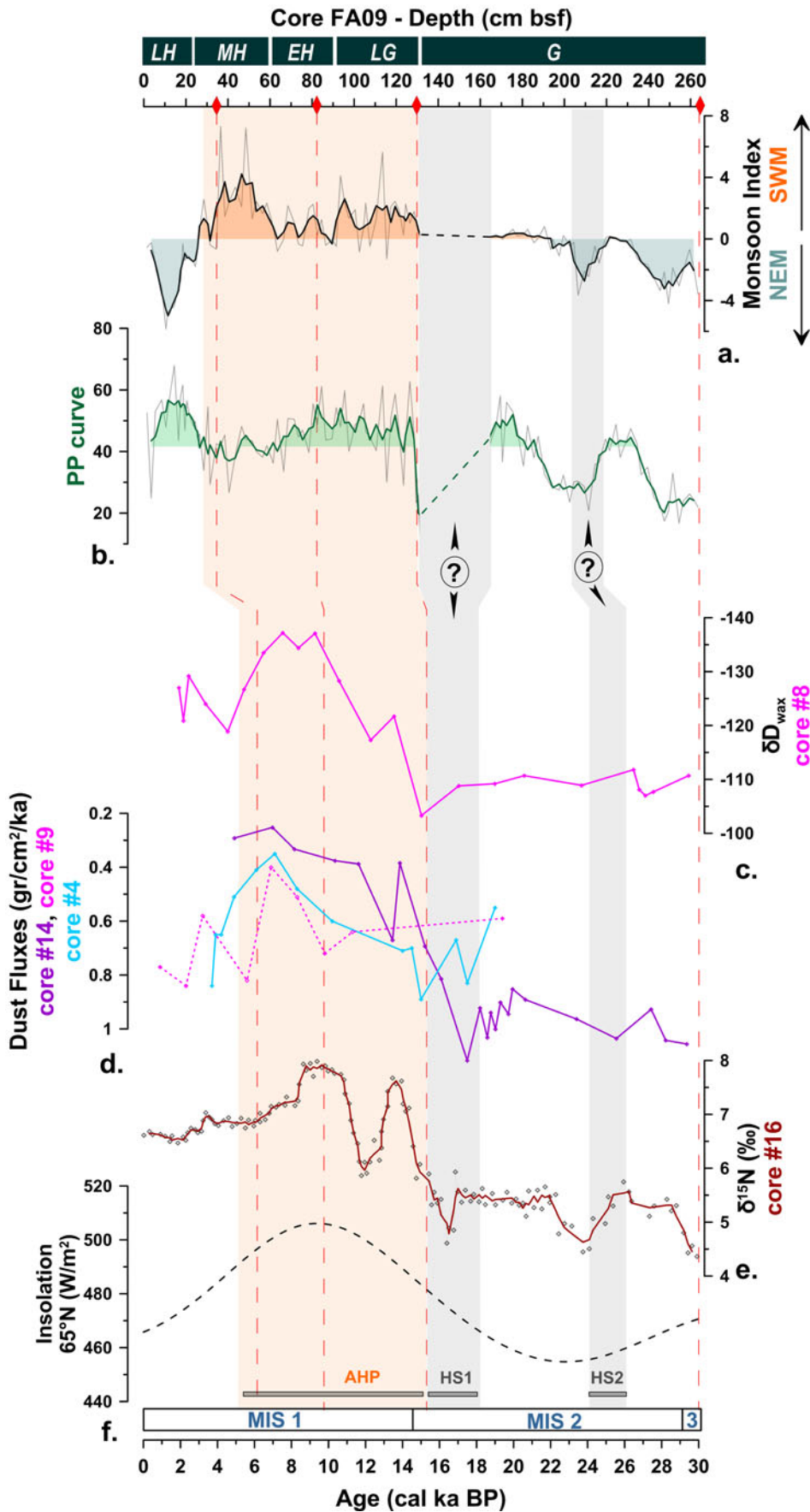


Figure 7 (a) Our proposed Monsoon Index based on planktic foraminifera associations in core FA09. (b) Paleoproductivity (PP) curve in FA09. (c) The δD_{wax} record of core #8 (after Tierney et al., 2017). (d) Dust fluxes (gr/cm²/ka) in the central Red Sea (core #4; Palchan and Torfstein, 2019), Gulf of Aden (core #9; Palchan and Torfstein, 2019), and northwestern Arabian Sea (core #14; Pourmand et al., 2007). (e) Denitrification Index ($\delta^{15}N$) in the northwestern Arabian Sea (core #16; Ivanochko et al., 2005). (f) Northern Hemisphere summer insolation (Laskar et al., 2004). The FA09 data are presented depth-wise (top x axis). The interval of SWM dominance (orange-shaded) coincides with the last “African Humid Period” (Shanahan et al., 2015; Ehrmann et al., 2017), and is sufficiently addressed by the calibrated dates in FA09. Heinrich stadials 1 and 2 (HS1, HS2) are noted (after Sanchez-Goni and Harrison, 2010). Question marks indicate the potential correlation between the HS and the FA09 records. The top horizontal bars represent glacial (G), late glacial (LG), Early Holocene (EH), Middle Holocene (MH), and Late Holocene (LH) chronostratigraphic intervals; bsf = below sea floor.

control in that interval is weak, it is quite rational to propose that it most likely corresponds to the MIS2 sea level lowstand (ca. 22–15 ka) (Fig. 5a), when the sea level drop would have instigated limited intrusions of fertile GoA and NWArs water masses into the Red Sea, leading to highly stressed conditions for the planktic assemblages. After ca. 15 ka and the onset of the late glacial period, the large differences of FA09 $\delta^{13}\text{C}$ record with those of GoA and NWArs possibly imply that local upwelling (previously discussed) was more effective than the influence of fertile intrusions in the Farasan Archipelago.

The SST record

Transition from cold climatic conditions of the glacial interval to warm conditions of the Holocene is reflected accordingly in the SST_{ANN} proxy of FA09. The SST records of southern Red Sea (FA09), GoA (core #8; Tierney *et al.*, 2017), and NWArs (cores #11, 12, 14; Rostek *et al.*, 1997; Pourmand *et al.*, 2007; Böll *et al.*, 2015) are sufficiently comparable in terms of trend and value range (mainly between 21–29°C), implying a continuous interaction over the last 30 ka (Fig. 6a). The total glacial-interglacial shift in the southern Red Sea is up to +3°C, and appears quite high in relation to that in the Arabian Sea (~+1.5 °C). Additionally, previous studies from the central and northern Red Sea have suggested a SST increase in the range of 4–5°C after the Holocene transition (Arz *et al.*, 2003b; Siddall *et al.*, 2003). This notable temperature rise of the Red Sea during solar insolation reinforcement reflects the sensitivity of the basin to sea surface warming, which is also observed in the present day (Chaidez *et al.*, 2017).

The SSS record

In the Red Sea, the major effect of the glacial-to-interglacial shift is reflected in the paleosalinity variation within the basin and is attributed to the sea level change. Several studies from the central and northern Red Sea found that during the last glacial lowstand seawater salinities would have been >50 psu as a result of high evaporation rates and a drastic reduction in the Red Sea-Indian Ocean water exchange (Thunell *et al.*, 1988; Almogi-Labin *et al.*, 1996; Hemleben *et al.*, 1996; Rohling *et al.*, 1998; Fenton *et al.*, 2000; Arz *et al.*, 2003b). The FA09 SSS_{ANN} record suggests that glacial salinities did not exceed 39 psu (Fig. 6b). This, together with the constant presence of planktic foraminifera throughout our record (including the low-abundance interval at 130–164 cm), suggests that the southern Red Sea remained connected with open ocean at least over the last 30 ka. Therefore, our data confirm the studies of Fenton *et al.* (2000) and Biton *et al.* (2008) who claimed that during the last glacial maximum (LGM), salinity at the southern Red Sea would have been relatively low due to the direct influence of GoA inflows, even in a restricted mode at that time. Accordingly, planktic foraminifera survived the glacial salinities in the southern sector (Fig. 5f), in contrast with the rest of the basin where aplanktonic conditions prevailed (Rohling *et al.*, 1998; Fenton *et al.*, 2000).

SSS_{ANN} lowering in our record after 15 ka (Fig. 6b) marks the termination of high glacial salinities in the Red Sea as a result of deglacial sea level rise (Cronin, 2012; Grant *et al.*, 2012), which forced an increased volume of less-saline water masses from the Arabian Sea to enter the basin (Thunell *et al.*, 1988; Arz *et al.*, 2003b). Moving onwards, comparison of the FA09 SSS_{ANN} record with SSS reconstruction of Arz *et al.* (2003a, b) for the northern Red Sea (core #6) (Fig. 6b) reveals common salinity values during the Early Holocene, before a drastic deviation between the

southern and northern sectors of the Red Sea appears after ca. 7 ka. Subsequently, the north-south SSS difference of the last 6 ka resembles the present day (Table 2). The Holocene SSS trend between the northern and southern Red Sea sectors ties well with the aforementioned $\delta^{18}\text{O}$ variation (Fig. 5c), thus further supporting a pattern of relatively similar sea water conditions throughout the Red Sea, which was terminated along with the southward migration of the ITCZ.

Monsoon variability and paleoenvironmental alternations over the last 30 ka imprinted on planktic foraminiferal assemblages

The ecological interpretation of the faunal four-factor model implies coupling of the planktic foraminifera associations with SAMS variation (see Supplementary file 5 for details). It is most probable that the first two factors indicate a dominant SWM circulation, while factors 3 and 4 combine assemblages that imply a rather strong NEM influence on the Arabian Sea-Red Sea water exchange system. In that sense, we propose that the difference between the sum of the first two factor scores (FS1 + FS2) and the sum of the latter two (FS3 + FS4) constitutes a “Monsoon Index” for the southern Red Sea oceanographic conditions, indicating a dominant SWM influence (positive values) or NEM influence (negative values) (Fig. 7a). Nevertheless, no estimates can be made for the 130–164 cm interval due to the high negative scores of all factors.

Comparison of the proposed Monsoon Index with the predicted variation of the summer insolation index (65°N; Laskar *et al.*, 2004) shows broadly similar trends for most of the last 30 ka (Fig. 7a, f), suggesting that the distribution of planktic foraminifera assemblages at the core site is coupling with variation of the SAMS. Furthermore, similarities are also observed between this index and the index of surface productivity (PP curve; Fig. 7b), suggesting that the SAMS is a considerable regulator for surface productivity levels in the southern Red Sea.

Our Monsoon Index depicts a prominent SWM dominance for the late glacial and Early–Middle Holocene, which is in phase with increased surface productivity in the southern Red Sea (Fig. 7a, b). Several studies from the Arabian and Red Sea confirm the prevalence of particularly humid conditions associated with enhanced SWM winds for that time (Fig. 7c–e). Pourmand *et al.* (2007) and Palchan and Torfstein (2019) reported a substantial decrease of dust fluxes in the NWArs (core #14), GoA (core #9), and central Red Sea (core #4) (Fig. 7d) regions, while Tierney *et al.* (2017) suggested a shift to more humid conditions in the GoA, imprinted as a notable decreasing trend in the $\delta\text{D}_{\text{wax}}$ values of core #8 (Fig. 7c). In addition, this period coincides with the last “African Humid Period” (AHP)—a period of high humidity and heavy rainfall across a wide area of North Africa (Shanahan *et al.*, 2015; Ehrmann *et al.*, 2017). The dominance of the SWM winds also induced high productivity levels in the NWArs; Ivanochko *et al.* (2005) recorded a major rise of denitrification ($\delta^{15}\text{N}$) in NWArs (core #16), indicating increased productivity related to SWM-driven upwelling (Fig. 7e). Therefore, intrusion of Arabian Sea nutrient-rich inflows and increased freshwater input, all related to the dominance of SWM winds, seem to have bolstered surface productivity in the southern Red Sea during this period. The signal of coupling between increased surface productivity and the prevalence of SWM winds, though attenuated in relation to the above discussed period, was occasionally observed within the glacial period as well, at ~165–180 cm and 220–236 cm in FA09 (Fig. 7a, b). In that context, it is notable

that several studies report occasional short-term SWM reinforcement during the glacial period (30–15 ka). In these studies, decline of the NEM winds and/or intensification of the SWM winds in the (discussed) glacial period is documented by relatively high marine productivity and increased upwelling in NWARs (Naidu and Malmgren, 1996; Schulz et al., 2002; Singh et al., 2016).

In contrast to the above, the planktic foraminifera associations of FA09 suggest low surface productivity levels during times of NEM dominance (as predicted by our proposed Monsoon Index) (Fig. 7a, b). This coupling between low surface productivity and the dominance of NEM winds is strong within most of the glacial period. It also is in agreement with several studies from the GoA and NWARs, which suggest that during glacial times NEM winds were dominant and associated with low marine productivity (Fontugne and Duplessy, 1986; Almogi-Labin et al., 2000; Pourmand et al., 2007; Böll et al., 2015). Therefore, the intrusion of nutrient-poor waters from the Arabian Sea, as well as the low freshwater discharges in the basin caused by increased aridity, may have reduced the surface productivity levels in the southern Red Sea during times of NEM dominance.

Enhanced NEM winds are also recorded on shorter timescales in Arabian Sea sediment records (Singh et al., 2011; Deplazes et al., 2014; Böll et al., 2015), and these are associated with periods of strong NEM winds driven by the southward migration and intensification of the mid-latitude westerlies. These periods, which date to ca. 25–24 ka and 17–15 ka, agree in age with the onset of Heinrich stadials 2 (HS2; 26.5–24.3 ka) and 1 (HS1; 18–15.6 ka) (Sanchez-Goni and Harrison, 2010). In our proxies, the two intervals that combine reductions in temperature (SST_{ANN}) and surface productivity at 130–164 cm and 200–220 cm may correspond to these periods (Figs. 6a, 7b).

The lower of the aforementioned intervals corresponds to a clear reinforcement of the NEM winds in the Monsoon Index of FA09 (Fig. 7a). On the other hand, our Monsoon Index does not apply to the upper interval (130–164 cm) owing to the drastic reduction of planktic foraminifera numbers (Figs. 3a, 5f). Notably, this major decrease ties well with previous findings in cores from the southern Red Sea basin and suggests an age close to that of HS1. Locke and Thunell (1988) detected a pronounced reduction of the planktic foraminiferal assemblages just after 18 ka in core #2 (Fig. 1a) while Fenton et al. (2000) detected a strong decrease in core #1 (Fig. 1a) that developed after 20 ka.

A combination of restricted intrusion of GoA and NWARs waters, along with decreased surface productivity under a dominant NEM system, is likely the key scenario that would generate faunal stress in the southern Red Sea. Previous studies have demonstrated that during Heinrich stadial 1, widespread aridity had prevailed in the Arabian and Red Sea areas associated with remarkably strong NEM winds and seriously declined SWM (Schulz et al., 2002; Arz et al., 2003b; Ivanochko et al., 2005; Pourmand et al., 2007; Singh et al., 2011; Deplazes et al., 2014; Palchan and Torfstein, 2019). Hence, it is most likely that arid conditions would have prevented fertile freshwater input while, at the same time, strong NEM winds forced inflows of nutrient-poor waters into the southern Red Sea. These inflows from the Arabian Sea would have been rather restricted due to low sea level at the time (Fig. 5a). Moreover, the low sea level further deteriorated environmental conditions, inducing high SSS in the southern Red Sea area (Fig. 4d). Therefore, highly saline and oligotrophic surface waters would have been unfavorable for planktic

foraminifera. The overall outcome of these environmental circumstances is also depicted in the textural characteristics of FA09 sediments (Lithological Unit B, Fig. 2), principally represented by a substantial color change.

An additional process that could partly explain the relationship between NEM winds and surface productivity in the southern Red Sea regards local oceanographic features. Today, very close to the core site, an anticyclonic eddy is observed (Sofianos and Johns, 2007; Yao et al., 2014; Abdulla et al., 2018). It is one among numerous anticyclones that prevail along the Red Sea, mostly in winter time, and probably relates to coastal mountain-gap wind-jets that frequently blow across the longitudinal axis of the Red Sea (Jiang et al., 2009). Assuming that the oceanographic regime of the southern Red Sea during winter season was similar in the past, intensification of that eddy under a strong and prolonged NEM system could have displaced the already nutrient-poor water deeper in the water column, reducing the surface productivity.

Beyond the above, we observe that, for the period after 5 ka, the signal of surface productivity does not follow the predicted variation of SAMS (Fig. 7a, b), as was discussed previously. Our Monsoon Index suggests prevalent NEM winds for that time (Fig. 7a). Indeed, decreasing insolation in the northern Hemisphere during the Middle–Late Holocene caused a weakening of the SWM, thus favoring establishment of more arid conditions in the area, associated with enhanced NEM winds (Overpeck et al., 1996; Fleitmann et al., 2007; Das et al., 2017). In addition, records from the GoA suggest a shift to less-humid conditions (Tierney et al., 2017) and increased dust fluxes (Palchan and Torfstein, 2019) just after 5 ka (Fig. 7c, d).

However, unexpectedly high levels of surface productivity are captured at the core location for the Late Holocene (Fig. 7b). Records from the central Red Sea point indicate that as well; Edelman-Furstenberg et al. (2009) suggested an increase in phytoplankton concentration in core #5 between 3.5–2 ka, while Siccha et al. (2009) estimated elevated concentrations of chlorophyll *a* for the same period in core #3, based on combined transfer function approaches using planktic foraminifera data. The above agree with observations of present-day conditions. Raitos et al. (2015) reported an increase in the concentration of chlorophyll *a* and the duration of the phytoplankton growing season in the Red Sea during the NEM season, linked with strengthened, fertile GASW intrusions. It is possible that this mechanism was active during the discussed interval, reinforcing the surface productivity in the southern and central Red Sea. Raitos et al. (2015) also declared that this process coincides with prolonged positive phases of the multivariate El Niño–Southern Oscillation (ENSO) Index. If this atmospheric circulation pattern also was active in the past, then this information could provide perspective for climate teleconnection of the Red Sea to the global ocean.

SUMMARY AND CONCLUSIONS

The combination of high-resolution micropaleontological (planktic foraminifera), stable isotope ($\delta^{18}\text{O}$, $\delta^{13}\text{C}$), and transfer function (Artificial Neural Networks) analyses of SST and SSS in sediment core FA09 from the southern Red Sea revealed the effects of sea level fluctuations and the South Asian Monsoon System (SAMS) on the oceanographic regime of the area for the last 30 ka. Additionally, our results were compared with other records from the Red Sea, Gulf of Aden (GoA) and

Northwestern Arabian Sea (NWARs), aiming to depict an overall paleoenvironmental assessment for these interacting regions.

We find that throughout the entire investigated interval, the Red Sea was connected to the Arabian Sea. Continuous intrusion of GoA inflows during the glacial section (30–15 ka) induced common SST variations in these regions and prevented hypersalinity in the southern Red Sea. The MIS2 sea level lowstand (ca. 22–15 ka) is characterized by the highest salinity (~38 psu) and lowest temperature (~23.5°C) estimates of the FA09 records. Deglacial sea level rise improved water mass exchange between the NWARs, GoA, and the entire Red Sea, while in the early Holocene, these three areas shared relatively similar surface-water conditions. Our data further support that sea level change is the dominant driver of Red Sea $\delta^{18}\text{O}$ variability for the last 30 ka, which shows a clear north-south differentiation.

Southwest monsoon (SWM) was dominant during the late glacial and Early–Middle Holocene, along with increased solar insolation in the Northern Hemisphere, which favored elevated surface productivity levels in the southern Red Sea. The combination of full water interaction with the Arabian Sea and strong SWM led to establishment of a dominant three-layered water circulation mode after 10 ka, with nutrient-rich GoA inflows controlling productivity in the southern Red Sea while prior to that (late glacial), local upwelling seems to have been the principal process explaining increased productivity.

Northeast monsoon (NEM) was enhanced during the glacial interval, associated with diminished productivity in the southern Red Sea. Yet, we highlight two (multi)millennial-scale periods of SST and surface productivity drop in the southern Red Sea, which potentially coincide with the onset of Heinrich stadials 2 and 1. The younger of these periods is marked by highly stressed environmental conditions and profound minimization of planktic foraminiferal assemblages, which probably resulted from restricted GoA inflow and low productivity under strong NEM circulation. During the Late Holocene, an intensification of the NEM is identified in association with increased phytoplankton masses in the southern and central Red Sea, suggesting a sufficient contribution of the NEM to the surface productivity levels of that period.

The present study shows that the relatively shallow shelf sediments have proved to be excellent paleo-archives and captured several climatic events since the final phase of MIS3. We thus emphasize the direct response of the dynamic shelf to climate-driven forces and underline the need for more systematic paleoceanographic research in similar environments throughout the world ocean, characterized by high sensitivity to sea level changes and alternating circulation patterns.

Acknowledgments. We thank the Saudi Commission for Tourism and National Heritage (SCTH) and the Department of General Survey of the Ministry of Defense for permission to undertake the fieldwork. S. Sergiou thanks the General Secretariat for Research and Technology (GSRT) and the Hellenic Foundation for Research and Innovation (HFRI) for funding support. We also thank the crew of the R/V AEGAEON for implementation of the coring survey. Finally, we are thankful to Dr. B. Mauz and Dr. D. Booth of the editorial board and the two anonymous reviewers for their efforts in reading the manuscript and making valuable comments and suggestions for its improvement. This paper is DISPERSE contribution no. 63.

Supplementary Material. To view the supplementary material for this article, please visit: <https://doi.org/10.1017/qua.2022.16>

Financial Support. This research was funded by the European Research Council through ERC Advanced Grant 269586 “DISPERSE: Dynamic

Landscapes, Coastal Environments and Human Dispersals” under the ‘Ideas’ Specific Programme of the Seventh Framework Programme.

Declaration of Competing Interest. The authors declare that they have no competing financial interests that could have appeared to influence the work reported in this paper.

REFERENCES

- Abdulla, C.P., Alsaafani, M.A., Alraddadi, T.M., Albarakati, A.M., 2018. Mixed layer depth variability in the Red Sea. *Ocean Science* **14**, 563–573.
- Al-Mikhlafi, A.S., Hibbert, F.D., Edwards, L.R., Cheng, H., 2021. Holocene relative sea-level changes and coastal evolution along the coastlines of Kamaran Island and As-Salif Peninsula, Yemen, southern Red Sea. *Quaternary Science Reviews* **252**, 106719. <https://doi.org/10.1016/j.quascirev.2020.106719>.
- Almogi-Labin, A., Hemleben, C., Meischner, D., Erlenkeuser, H., 1991. Paleoenvironmental events during the last 13000 years in the central Red Sea as recorded by Pteropoda. *Paleoceanography* **6**, 83–98.
- Almogi-Labin, A., Hemleben, C., Meischner, D., Erlenkeuser, H., 1996. Response of Red Sea deep-water agglutinated foraminifera to water-mass changes during the late Quaternary. *Marine Micropaleontology* **28**, 283–297.
- Almogi-Labin, A., Schmiedl, G., Hemleben, C., Siman-tov, R., Segl, M., Meischner, D., 2000. The influence of the NE winter monsoon on productivity changes in the Gulf of Aden, NW Arabian Sea, during the last 530 ka as recorded by foraminifera. *Marine Micropaleontology* **40**, 295–319.
- Anderson, D.M., Prell, W.L., 1991. Coastal upwelling gradient during the late Pleistocene. *Proceedings of the Ocean Drilling Program, Scientific Results* **117**, 265–276.
- Anderson, D.M., Prell, W.L., 1992. The structure of the southwest monsoon winds over the Arabian Sea during the late Quaternary: observations, simulations, and marine geologic evidence. *Journal of Geophysical Research* **97**, 15481–15487.
- Arz, H.W., Lamy, F., Pätzold, J., Müller, P., Prins, M., 2003a. Mediterranean Moisture Source for an Early-Holocene Humid Period in the Northern Red Sea. *Science* **300**, 118–121.
- Arz, H.W., Pätzold, J., Müller, P., 2003b. Influence of Northern Hemisphere climate and global sea level rise on the restricted Red Sea marine environment during termination I. *Paleoceanography* **18**, 1053. <https://doi.org/10.1029/2002PA000864>.
- Arz, H.W., Lamy, F., Pätzold, J., 2006. A pronounced dry event recorded around 4.2 ka in brine sediments from the northern Red Sea. *Quaternary Research* **66**, 432–441.
- Arz, H.W., Lamy, F., Ganopolski, A., Nowaczyk, N., Pätzold, J., 2007. Dominant Northern Hemisphere climate control over millennial-scale glacial sea-level variability. *Quaternary Science Reviews* **26**, 312–321.
- Auras-Schudnagies, A., Kroon, D., Ganssen, G., Hemleben, C., Van Hinte, J., 1989. Distributional pattern of planktonic foraminifera and pteropods in surface waters and top core sediments of the Red Sea, and adjacent areas controlled by the monsoonal regime and other ecological factors. *Deep-Sea Research Part A. Oceanographic Research Papers* **36**, 1515–1533.
- Badawi, A., 2015. Late Quaternary glacial/interglacial cyclicity models of the Red Sea. *Environmental Earth Sciences* **73**, 961–977.
- Bailey, G.N., Deves, M.H., Inglis, R.H., Meredith-Williams, M.G., Momber, G., Sakellariou, D., Sinclair, A.G.M., Rousakis, G., Ghamdi, S. Al, Alsharekh, A.M., 2015. Blue Arabia: Palaeolithic and underwater survey in SW Saudi Arabia and the role of coasts in Pleistocene dispersals. *Quaternary International* **382**, 42–57.
- Banerji, U.S., Arulbalaji, P., Padmalal, D., 2020. Holocene climate variability and Indian Summer Monsoon: an overview. *The Holocene* **30**, 744–773.
- Barrows, T.T., Juggins, S., 2005. Sea-surface temperatures around the Australian margin and Indian Ocean during the Last Glacial Maximum. *Quaternary Science Reviews* **24**, 1017–1047.
- Be, A.W.H., Tolderlund, D.S., 1971. Distribution and ecology of living planktonic foraminifera in surface waters of the Atlantic and Indian Oceans. In: Funnel, B.M., Riedel, W.R. (Eds.), *The Micropaleontology of Oceans*. Cambridge University Press, Cambridge, UK, pp. 105–149.

- Biton, E., Gildor, H., Peltier, W.R., 2008. Red Sea during the Last Glacial Maximum: implications for sea level reconstruction. *Paleoceanography* **23**, PA1214. <https://doi.org/10.1029/2007PA001431>.
- Böll, A., Schulz, H., Munz, P., Rixen, T., Gaye, B., Emeis, K., 2015. Contrasting sea surface temperature of summer and winter monsoon variability in the northern Arabian Sea over the last 25 ka. *Palaeoecology, Palaeoclimatology, Palaeoecology* **426**, 10–21.
- Caley, T., Malaizé, B., Zaragosi, S., Rossignol, L., Bourget, J., Eynaud, F., Martinez, P., Giraudeau, J., Charlier, K., Ellouz-Zimmermann, N., 2011. New Arabian Sea records help decipher orbital timing of Indo-Asian monsoon. *Earth and Planetary Science Letters* **308**, 433–444. <https://doi.org/10.1016/j.epsl.2011.06.019>
- Cayre, O., Beaufort, L., Vincent, E., 1999. Paleoproductivity in the equatorial Indian Ocean for the last 260,000 yr: a transfer function based on planktonic foraminifera. *Quaternary Science Reviews* **18**, 839–857.
- Chaidez, V., Dreano, D., Agusti, S., Duarte, C.M., Hoteit, I., 2017. Decadal trends in Red Sea maximum surface temperature. *Scientific Reports* **7**, 8144. <https://doi.org/10.1038/s41598-017-08146-z>
- Churchill, J.H., Bower, A.S., McCorkle, D.C., 2014. The transport of nutrient-rich Indian Ocean water through the Red Sea and into coastal reef systems. *Journal of Marine Research* **72**, 165–181.
- Clemens, S.C., Prell, W.L., 2003. A 350,000 year summer-monsoon multiproxy stack from the Owen Ridge, Northern Arabian Sea. *Marine Geology* **201**, 35–51.
- Conan, S.M., Brummer, G.A., 2000. Fluxes of planktic foraminifera in response to monsoonal upwelling on the Somalia Basin margin. *Deep-Sea Research* **47**, 2207–2227.
- Cronin, T.M., 2012. Rapid sea-level rise. *Quaternary Science Reviews* **56**, 11–30.
- Das, M., Singh, R.K., Gupta, A.K., Bhaumik, A.K., 2017. Holocene strengthening of the Oxygen Minimum Zone in the northwestern Arabian Sea linked to changes in intermediate water circulation or Indian monsoon intensity? *Palaeoecology, Palaeoclimatology, Palaeoecology* **483**, 125–135.
- Dasari, H.P., Langodan, S., Viswanadhapalli, Y., Valdamudi, B., Papadopoulos, V.P., Hoteit, I., 2018. ENSO influence on the interannual variability of the Red Sea. *International Journal of Climatology* **38**, 761–775.
- Demuth, H., Beale, M., Hagan, M., 2007. *Neural Network Toolbox User's Guide*. MathWorks, Natick, MA, USA.
- Deplazes, G., Lückge, A., Peterson, L.C., Timmermann, A., Hamann, Y., Hughen, K.A., Röhl, U., et al., 2013. Links between tropical rainfall and North Atlantic climate during the last glacial period. *Nature Geoscience* **6**, 213–217.
- Deplazes, G., Lückge, A., Stuut, J.W., Pätzold, J., Kuhlmann, H., Husson, D., Fant, M., Haug, G.H., 2014. Weakening and strengthening of the Indian monsoon during Heinrich events and Dansgaard-Oeschger oscillations. *Paleoceanography* **29**, 99–114.
- Donohoe, A., Marshall, J., Ferreira, D., Mcgee, D., 2013. The relationship between ITCZ location and cross-equatorial atmospheric heat transport: from the seasonal cycle to the Last Glacial Maximum. *Journal of Climate* **26**, 3597–3618.
- Dreano, D., Raitso, D.E., Gittings, J., Krokos, G., Hoteit, I., 2016. The Gulf of Aden intermediate water intrusion regulates the southern Red Sea summer phytoplankton blooms. *PLoS ONE* **11**, e0168440. <https://doi.org/10.1371/journal.pone.0168440>.
- Edelman-Furstenberg, Y., Almogi-Labin, A., Hemleben, C., 2009. Palaeoceanographic evolution of the central Red Sea during the Late Holocene. *The Holocene* **1**, 117–127.
- Ehrmann, W., Schmiedl, G., Beuscher, S., Kru, S., 2017. Intensity of African humid periods estimated from Saharan dust fluxes. *PLoS ONE* **12**, e0170989. <https://doi.org/10.1371/journal.pone.0170989>.
- Emeis, K.C., Anderson, D.M., Doose, H., Kroon, D., Schulz-Bull, D., 1995. Sea-surface temperatures and the history of monsoon upwelling in the northwest Arabian Sea during the last 500,000 years. *Quaternary Research* **43**, 355–361.
- Fenton, M., Geiselhart, S., Rohling, E.J., Hemleben, C., 2000. A planktonic zones in the Red Sea. *Marine Micropaleontology* **40**, 277–294.
- Fleitmann, D., Burns, S.J., Mangini, A., Mudelsee, M., Kramers, J., Villa, I., Neff, U., et al., 2007. Holocene ITCZ and Indian monsoon dynamics recorded in stalagmites from Oman and Yemen (Socotra). *Quaternary Science Reviews* **26**, 170–188.
- Fontugne, M.R., Duplessy, J., 1986. Variations of the monsoon regime during the upper Quaternary: evidence from carbon isotopic record of organic matter in North Indian Ocean sediment cores. *Palaeoecology, Palaeoclimatology, Palaeoecology* **56**, 69–88.
- Ganssen, G.M., Peeters, F.J.C., Metcalfe, B., Anand, P., Jung, S.J.A., Kroon, D., Brummer, G.A., 2011. Quantifying sea surface temperature ranges of the Arabian Sea for the past 20 000 years. *Climate of the Past* **7**, 1337–1349.
- Gaye, B., Böll, A., Segsneider, J., Burdanowitz, N., Emeis, K., Ramaswamy, V., Lahajnar, N., Lückge, A., Rixen, T., 2018. Glacial-interglacial changes and Holocene variations in Arabian Sea denitrification. *Biogeosciences* **15**, 507–527.
- Gebler, D., Kolada, A., Pasztaleniec, A., 2020. Modelling of ecological status of Polish lakes using deep learning techniques. *Environmental Science and Pollution Research* **28**, 5383–5397.
- Geraga, M., Sergiou, S., Sakellariou, D., Rohling, E., 2019. Results of micropalaeontological analyses on sediment core FA09 from the southern Red Sea continental shelf. In: Rasul, N., Stewart, I. (Eds.), *Geological Setting, Palaeoenvironment and Archaeology of the Red Sea*. Springer, Cham, pp. 709–723.
- Gittings, J.A., Raitso, D.E., Racault, M., Brewin, R.J.W., Pradhan, Y., Sathyendranath, S., Platt, T., 2017. Remote sensing of environment seasonal phytoplankton blooms in the Gulf of Aden revealed by remote sensing. *Remote Sensing of Environment* **189**, 56–66.
- Grant, K.M., Rohling, E.J., Ayalon, A., Ramsey, C.B., Satow, C., Roberts, A.P., 2012. Rapid coupling between ice volume and polar temperature over the past 150,000 years. *Nature* **491**, 744–747.
- Gupta, A.K., Anderson, D.M., Overpeck, J.T., 2003. Abrupt changes in the Asian Southwest Monsoon during the Holocene and their links to the North Atlantic Ocean. *Nature* **421**, 354–357.
- Hadjisolomou, E., Stefanidis, K., Papatheodorou, G., Papastergiadou, E., 2016. Assessing the contribution of the environmental parameters to eutrophication with the use of the “PaD” and “PaD2” methods in a hypereutrophic lake. *International Journal of Environmental Research and Public Health* **13**, 764. <https://doi.org/10.3390/ijerph13080764>
- Hair, J., Black, W., Babin, B., Anderson, R., Tatham, R., 2006. *Multivariate Data Analysis (6th ed.)*. Pearson Prentice Hall, Upper Saddle River, NJ.
- Hartman, A., Torfstein, A., Almogi-Labin, A., 2020. Climate swings in the northern Red Sea over the last 150,000 years from ϵNd and Mg/Ca of marine sediments. *Quaternary Science Reviews* **231**, 106205. <https://doi.org/10.1016/j.quascirev.2020.106205>
- Hayes, A., Kucera, M., Kalle, N., Shaffi, L., Rohling, E.J., 2005. Glacial Mediterranean sea surface temperatures based on planktonic foraminiferal assemblages. *Quaternary Science Reviews* **24**, 999–1016.
- Heaton, T.J., Köhler, P., Butzin, M., Bard, E., Reimer, R.W., Austin, W.E.N., Ramsey, C.B., et al., 2020. Marine20—the marine radiocarbon age calibration curve (0–55,000 cal BP). *Radiocarbon* **62**, 779–820.
- Hemleben, C., Meischner, D., Zahn, R., Almogi-Labin, A., Erlenkeuser, H., Hiller, B., 1996. Three hundred eighty thousand year long stable isotope and faunal records from the Red Sea: influence of global sea level change on hydrography. *Paleoceanography* **11**, 147–156.
- Hoyle, T.M., Bista, D., Flecker, R., Krijgsman, W., Sangiorgi, F., 2021. Climate-driven connectivity changes of the Black Sea since 430 ka: testing a dual palynological and geochemical approach. *Palaeoecology, Palaeoclimatology, Palaeoecology* **561**, 110069. <https://doi.org/10.1016/j.palaeo.2020.110069>
- Ishikawa, S., Oda, M., 2007. Reconstruction of Indian monsoon variability over the past 230,000 years: planktic foraminiferal evidence from the NW Arabian Sea open-ocean upwelling area. *Marine Micropaleontology* **63**, 143–154.
- Ivanochko, T.S., Ganeshram, R.S., Brummer, G.A., Ganssen, G., Jung, S.J.A., Moreton, S.G., Kroon, D., 2005. Variations in tropical convection as an amplifier of global climate change at the millennial scale. *Earth and Planetary Science Letters* **235**, 302–314.
- Ivanova, E., Schiebel, R., Deo, A., Schmiedl, G., Niebler, H., Hemleben, C., 2003. Primary production in the Arabian Sea during the last 135 000 years. *Palaeoecology, Palaeoclimatology, Palaeoecology* **197**, 61–82.

- Jiang, H., Farrar, J.T., Beardsley, R.C., Chen, R., Chen, C., 2009. Zonal surface wind jets across the Red Sea due to mountain gap forcing along both sides of the Red Sea. *Geophysical Research Letters* **36**, L19605. <https://doi.org/10.1029/2009GL040008>.
- Joseph, P., Eischeid, J., Pyle, R., 1994. Interannual variability of the onset of the Indian Summer Monsoon and its association with atmospheric features, El Niño, and sea surface temperature anomalies. *Journal of Climate* **7**, 81–105.
- Kathayat, G., Cheng, H., Sinha, A., Spötl, C., Edwards, R.L., Zhang, H., Li, X., et al., 2016. Indian monsoon variability on millennial-orbital timescales. *Scientific Reports* **6**, 24374. <https://doi.org/10.1038/srep24374>.
- Kite, M.E., Whitley, B.E., 2018. Factor analysis, path analysis, and structural equation modeling. In: Kite, M.E., Whitley, B.E., *Principles of Research in Behavioral Science*, 4th ed. Jones and Barlett Publishers, New York. <https://doi.org/10.4324/9781315450087-12>.
- Kroon, D., Ganssen, G., 1989. Northern Indian Ocean upwelling cells and the stable isotope composition of living planktonic foraminifers. *Deep-Sea Research* **36**, 1219–1236.
- Kürten, B., Zarokanellos, N.D., Devassy, R.P., El-Sherbiny, M.M., Struck, U., Capone, D.G., Schulz, I.K., Al-Aidaros, A.M., Irigoien, X., 2019. Seasonal modulation of mesoscale processes alters nutrient availability and plankton communities in the Red Sea. *Progress in Oceanography* **173**, 238–255.
- Lambeck, K., Purcell, A., Flemming, N.C., Vita-Finzi, C., Alsharekh, A.M., Bailey, G.N., 2011. Sea level and shoreline reconstructions for the Red Sea: isostatic and tectonic considerations and implications for hominin migration out of Africa. *Quaternary Science Reviews* **30**, 3542–3574.
- Laskar, J., Robutel, P., Joutel, F., Gastineau, M., Correia, A.C.M., Levrard, B., 2004. A long-term numerical solution for the insolation quantities of the Earth. *Astronomy & Astrophysics* **428**, 261–285.
- Legge, H.L., Mutterlos, J., Arz, H.W., 2006. Climatic changes in the northern Red Sea during the last 22,000 years as recorded by calcareous nannofossils. *Paleoceanography* **21**, PA1003. <https://doi.org/10.1029/2005PA001142>.
- Leuschner, D.C., Sirocko, F., 2000. The low-latitude monsoon climate during Dansgaard-Oeschger cycles and Heinrich Events. *Quaternary Science Reviews* **19**, 243–254.
- Leuschner, D.C., Sirocko, F., 2003. Orbital insolation forcing of the Indian Monsoon—a motor for global climate changes? *Palaeogeography, Palaeoclimatology, Palaeoecology* **197**, 83–95.
- Li, W., El-Askary, H., Qurban, M.A., Proestakis, E., Id, E.M., Piechota, T., Manikandan, K.P., 2018. An assessment of atmospheric and meteorological factors regulating Red Sea phytoplankton growth. *Remote Sensing* **10**, 673. <https://doi.org/10.3390/rs10050673>.
- Lisiecki, L.E., Raymo, M.E., 2005. A Pliocene–Pleistocene stack of 57 globally distributed benthic $\delta^{18}\text{O}$ records. *Paleoceanography* **20**, PA1003. <https://doi.org/10.1029/2004PA001071>.
- Liu, W., Chen, W., 2012. Prediction of water temperature in a subtropical sub-alpine lake using an artificial neural network and three-dimensional circulation models. *Computers & Geosciences* **45**, 13–25.
- Locarnini, R.A., Mishonov, A., Baranova, O.K., Boyer, T., Zweng, M., Garcia, H., Reagan, J., et al., 2018. World ocean atlas 2018, volume 1: temperature. In: Mishonov, A. (Tech. Ed.), *NOAA Atlas NESDIS 81*. Silver Spring, Maryland, NOAA, 52 pp.
- Locke, S., Thunell, R.C., 1988. Paleoceanographic record of the last glacial/interglacial cycle in the Red Sea and Gulf of Aden. *Palaeogeography, Palaeoclimatology, Palaeoecology* **64**, 163–187.
- Mackensen, A., Schmiedl, G., 2019. Stable carbon isotopes in paleoceanography: atmosphere, oceans, and sediments. *Earth-Science Reviews* **197**, 102893. <https://doi.org/10.1016/j.earscirev.2019.102893>.
- Malmgren, B.A., Nordlund, U., 1997. Application of artificial neural networks to paleoceanographic data. *Palaeogeography, Palaeoclimatology, Palaeoecology* **136**, 359–373.
- Mazzulo, J., Graham, A.G., 1988. Handbook for shipboard sedimentologists. *Ocean Drilling Program, Technical Note 8*, 1–67.
- McCreary, J., Kohler, K., Hood, R.R., Olson, D., 1996. A four-component ecosystem model of biological activity in the Arabian Sea. *Progress in Oceanography* **37**, 193–240.
- McGee, D., Donohoe, A., Marshall, J., Ferreira, D., 2014. Changes in ITCZ location and cross-equatorial heat transport at the Last Glacial Maximum, Heinrich Stadial 1, and the mid-Holocene. *Earth and Planet. Science Letters* **390**, 69–79.
- McHugh, C.M.G., Gurung, D., Giosan, L., Ryan, W.B.F., Mart, Y., Sancar, U., Burckle, L., Çagatay, M.N., 2008. The last reconnection of the Marmara Sea (Turkey) to the World Ocean: a paleoceanographic and paleoclimatic perspective. *Marine Geology* **255**, 64–82.
- McNeill, L.C., Shillington, D.J., Carter, G.D.O., Everest, J.D., Gawthorpe, R.L., Miller, C., Phillips, M.P., et al., 2019. High-resolution record reveals climate-driven environmental and sedimentary changes in an active rift. *Scientific Reports* **9**, 3116. <https://doi.org/10.1038/s41598-019-40022-w>.
- Munz, P.M., Siccha, M., Lückge, A., Böll, A., Kucera, M., Schulz, H., 2015. Decadal-resolution record of winter monsoon intensity over the last two millennia from planktic foraminiferal assemblages in the northeastern Arabian Sea. *The Holocene* **25**, 1756–1771.
- Munz, P.M., Steinke, S., Böll, A., Lückge, A., Groeneveld, J., Kucera, M., Schulz, H., 2017. Decadal resolution record of Oman upwelling indicates solar forcing of the Indian summer monsoon (9–6 ka). *Climate of the Past* **13**, 491–509.
- Naidu, P.D., 2004. Isotopic evidences of past upwelling intensity in the Arabian Sea. *Global and Planetary Change* **40**, 285–293.
- Naidu, P.D., Malmgren, B., 2005. Seasonal sea surface temperature contrast between the Holocene and last glacial period in the western Arabian Sea (Ocean Drilling Project Site 723A): modulated by monsoon upwelling. *Paleoceanography* **20**, PA1004. <https://doi.org/10.1029/2004PA001078>.
- Naidu, P.D., Malmgren, B.A., 1996. A High-resolution record of late Quaternary upwelling along the Oman Margin, Arabian Sea based on planktonic foraminifera. *Paleoceanography* **11**, 129–140.
- Overpeck, J., Anderson, D., Trumbore, S., Prell, W., 1996. The southwest Indian Monsoon over the last 18 000 years. *Climate Dynamics* **12**, 213–225.
- Palchan, D., Torfstein, A., 2019. A drop in Sahara dust fluxes records the northern limits of the African Humid Period. *Nature Communications* **10**, 3803. <https://doi.org/10.1038/s41467-019-11701-z>.
- Papatheodorou, G., Demopoulou, G., Lambrakis, N., 2006. A long-term study of temporal hydrochemical data in a shallow lake using multivariate statistical techniques. *Ecological Modelling* **193**, 759–776.
- Peeters, F.J.C., Brummer, G.A., Ganssen, G., 2002. The effect of upwelling on the distribution and stable isotope composition of *Globigerina bulloides* and *Globigerinoides ruber* (planktic foraminifera) in modern surface waters of the NW Arabian Sea. *Global and Planetary Change* **34**, 269–291.
- Pourmand, A., Marcantonio, F., Bianchi, T.S., Canuel, E.A., Waterson, E.J., 2007. A 28-ka history of sea surface temperature, primary productivity and planktonic community variability in the western Arabian Sea. *Paleoceanography* **22**, PA4208. <https://doi.org/10.1029/2007PA001502>.
- Pujol, C., Vergnaud-Grazzini, C., 1995. Distribution patterns of live planktic foraminifers as related to regional hydrography and productive systems of the Mediterranean Sea. *Marine Micropaleontology* **25**, 187–217.
- Raitsos, D.E., Yi, X., Platt, T., Racault, M., Brewin, R.J.W., Pradhan, Y., Papadopoulos, V.P., Sathyendranath, S., Hoteit, I., 2015. Monsoon oscillations regulate fertility of the Red Sea. *Geophysical Research Letters* **42**, 855–862.
- Reiss, Z., Luz, B., Almogi-Labin, A., Halicz, E., Winter, A., Wolf, M., 1980. Late Quaternary paleoceanography of the Gulf of Aqaba (Elat), Red Sea. *Quaternary Research* **14**, 294–308.
- Reyment, R.A., Joreskog, K.G., 1996. *Applied Factor Analysis in the Natural Sciences*. Cambridge University Press, Cambridge, UK.
- Roberts, A.P., Rohling, E.J., Grant, K.M., Larrasoana, J.C., Liu, Q., 2011. Atmospheric dust variability from Arabia and China over the last 500,000 years. *Quaternary Science Reviews* **30**, 3537–3541.
- Rohling, E.J., 1994. Glacial conditions in the Red Sea. *Paleoceanography* **9**, 653–660.
- Rohling, E.J., Cooke, S., 1999. Stable oxygen and carbon isotopes in foraminiferal carbonate shells. In: Sen Gupta, B.K. (Ed.), *Modern Foraminifera*. Springer, New York, Dordrecht. https://doi.org/10.1007/0-306-48104-9_14.
- Rohling, E.J., Fenton, M., Jorissen, F.J., Bertrand, P., Ganssen, G., Caulet, J.P., 1998. Magnitudes of sea-level lowstands of the past 500,000 years. *Nature* **394**, 162–165.
- Rohling, E.J., Grant, K., Hemleben, C., Kucera, M., Roberts, A.P., Schmeltzer, I., Schulz, H., Siccha, M., Siddall, M., Trommer, G., 2008.

- New constraints on the timing of sea level fluctuations during early to middle Marine Isotope Stage 3. *Paleoceanography* **23**, PA3219. <https://doi.org/10.1029/2008PA001617>.
- Rostek, F., Bard, E., Beaufort, L.U.C., Sonzogni, C., Ganssent, G., 1997. Sea surface temperature and productivity records for the past 240 kyr in the Arabian Sea. *Deep-Sea Research* **44**, 1461–1480.
- Saher, M.H., Jung, S.J.A., Elderfield, H., Greaves, M.J., Kroon, D., 2007. Sea surface temperatures of the western Arabian Sea during the last deglaciation. *Paleoceanography* **22**, PA2208. <https://doi.org/10.1029/2006PA001292>.
- Sanchez-Goni, M., Harrison, S., 2010. Millennial-scale climate variability and vegetation changes during the Last Glacial: Concepts and terminology. *Quaternary Science Reviews* **29**, 2823–2827.
- Sarkar, A., Pandey, P., 2015. River Water Quality Modelling using Artificial Neural Network Technique. *Aquatic Procedia* **4**, 1070–1077.
- Schiebel, R., Hemleben, C., 2017. *Planktic Foraminifers in the Modern Ocean*. Springer-Verlag Berlin, Heidelberg. <https://doi.org/10.1007/978-3-662-50297-6>.
- Schiebel, R., Zeltner, A., Treppke, U.F., Waniek, J.J., Rixen, T., Hemleben, C., 2004. Distribution of diatoms, coccolithophores and planktic foraminifers along a trophic gradient during SW monsoon in the Arabian Sea. *Marine Micropaleontology* **51**, 345–371.
- Schulz, H., Von Rad, U., Erlenkeuser, H., 1998. Correlation between Arabian Sea and Greenland climate oscillations of the past 110,000 years. *Nature* **393**, 54–57.
- Schulz, H., Von Rad, U., Ittekkot, V., 2002. Planktic foraminifera, particle flux and oceanic productivity off Pakistan, NE Arabian Sea: modern analogues and application to the palaeoclimatic record. In: Clift, P.D., Kroon, D., Gaedicke, C., Craig, J. (Eds.), *The Tectonic and Climatic Evolution of the Arabian Sea Region*. Geological Society, London, Special Publication **195**, 499–516.
- Shakun, J.D., Burns, S.J., Fleitmann, D., Kramers, J., Matter, A., Al-Subary, A., 2007. A high-resolution, absolute-dated deglacial speleothem record of Indian Ocean climate from Socotra Island, Yemen. *Earth and Planetary Science Letters* **259**, 442–456.
- Shanahan, T.M., McKay, N.P., Hughen, K.A., Overpeck, J.T., Otto-Bliesner, B., Heil, C.W., King, J., Scholz, C.A., Peck, J., 2015. The time-transgressive termination of the African Humid Period. *Nature Geoscience* **9**, 140–144.
- Siccha, M., Trommer, G., Schulz, H., Hemleben, C., Kucera, M., 2009. Factors controlling the distribution of planktonic foraminifera in the Red Sea and implications for the development of transfer functions. *Marine Micropaleontology* **72**, 146–156.
- Siddall, M., Smeed, D.A., Matthiesen, S., Rohling, E.J., 2002. Modelling the seasonal cycle of the exchange flow in Bab El Mandab (Red Sea). *Deep-Sea Research* **49**, 1551–1569.
- Siddall, M., Rohling, E.J., Almog-Labin, A., Hemleben, C., Meischner, D., Schmeltzer, I., Smeed, D.A., 2003. Sea-level fluctuations during the last glacial cycle. *Nature* **423**, 853–858.
- Siddall, M., Smeed, D.A., Hemleben, C., Rohling, E.J., Schmeltzer, I., Peltier, W.R., 2004. Understanding the Red Sea response to sea level. *Earth and Planetary Science Letters* **225**, 421–434.
- Singh, A.D., Jung, S.J.A., Darling, K., Ganeshram, R., Ivanochko, T., Kroon, D., 2011. Productivity collapses in the Arabian Sea during glacial cold phases. *Paleoceanography* **26**, PA3210. <https://doi.org/10.1029/2009PA001923>.
- Singh, A.K., Tiwari, M., Shrivastava, A., Sinha, D.K., 2016. Wind Strength Variability in the Western Arabian Sea since the Last Glacial Maximum: Southwest vs. Northeast Monsoon Modes. *Journal of Climate Change* **2**, 57–70.
- Sirocko, F., Gabre-Schonberg, D., McIntyre, A., Molino, B., 1996. Teleconnections between the subtropical monsoons and high-latitude climates during the last deglaciation. *Science* **272**, 526–529.
- Sirocko, F., Sarnthein, M., Erlenkeuser, H., 1993. Century-scale events in monsoonal climate over the past 24,000 years. *Nature* **364**, 322–324.
- Sofianos, S.S., Johns, W.E., 2007. Observations of the summer Red Sea circulation. *Journal of Geophysical Research* **112**, C06025. <https://doi.org/10.1029/2006JC003886>.
- Sofianos, S., Johns, W.E., 2015. Water mass formation, overturning circulation, and the exchange of the Red Sea with the adjacent basins. In: Rasul, N.M.A., Stewart, I.C.F. (Eds.), *The Red Sea The Formation, Morphology, Oceanography and Environment of a Young Ocean Basin*. Springer, Heidelberg, pp. 343–353.
- Sohlenius, G., Sternbeck, J., Andren, E., Westman, P., 1996. Holocene history of the Baltic Sea as recorded in a sediment core from the Gotland Deep. *Marine Geology* **134**, 183–201.
- Southon, J., Kashgarian, M., Fontugne, M., Metvier, B., Yim, W., 2002. Marine reservoir corrections for the Indian Ocean and southeast Asia. *Radiocarbon* **44**, 167–180.
- Stuiver, M., Reimer, P.J., Reimer, R.W., 2022. CALIB 8.2 (WWW program). <http://calib.org>.
- Thunell, R.C., Locke, S.M., Williams, D.F., 1988. Glacio-eustatic sea-level control on Red Sea salinity. *Nature* **334**, 601–604.
- Tierney, J.E., Peter, B., Zander, P.D., 2017. A climatic context for the out-of-Africa migration. *Geology* **45**, 1023–1026.
- Trommer, G., Siccha, M., Rohling, E.J., Grant, K., Meer, M.T.J., Van Der Schouten, S., Baranowski, U., Kucera, M., 2011. Sensitivity of Red Sea circulation to sea level and insolation forcing during the last interglacial. *Climate of the Past* **7**, 941–955.
- Trommer, G., Siccha, M., Rohling, E.J., Grant, K., Meer, M.T.J., Van Der Schouten, S., Hemleben, C., Kucera, M., 2010. Millennial-scale variability in Red Sea circulation in response to Holocene insolation forcing. *Paleoceanography* **25**, PA3203. <https://doi.org/10.1029/2009PA001826>.
- Walker, M.J.C., Berkelhammer, M., Bjork, S., Cwynar, L.C., Fisher, D.A., Long, A.J., Lowe, J.J., 2012. Formal subdivision of the Holocene Series/Epoch: a discussion paper by a working group of INTIMATE (integration of ice-core, marine and terrestrial records) and the Subcommission on Quaternary Stratigraphy (International Commission on Stratigraphy). *Journal of Quaternary Science* **27**, 649–659.
- Wang, Y., Cheng, H., Edwards, R.L., He, Y., Kong, X., An, Z., Wu, J., Kelly, M., Dykoski, C.A., Li, X., 2005. The Holocene Asian monsoon: links to solar changes and North Atlantic climate. *Science* **308**, 854–857.
- Woelk, S., Quadfasel, D., 1996. Renewal of deep water in the Red Sea during 1982–1987. *Journal of Geophysical Research* **101**, 18155–18165.
- Wolff, T., Grieger, B., Hale, W., Dürkoop, A., Mulitza, S., Pätzold, J., Wefer, G., 1999. On the reconstruction of paleosalinities. In: Fischer, G., Wefer, G. (Eds.), *Use of Proxies in Paleoceanography: Examples from the South Atlantic*. Springer, Berlin Heidelberg, pp. 207–228.
- WoRMS Editorial Board, 2021. *World Register of Marine Species*. <https://www.marinespecies.org> at VLIZ. [Accessed 2021-08-23]. <https://doi.org/10.14284/170>.
- Yao, F., Hoteit, I., Pratt, L., Bower, A.S., Zhai, P., Kohl, A., Gopalakrishnan, G., 2014. Seasonal overturning circulation in the Red Sea: 1. Model validation and summer circulation. *Journal of Geophysical Research: Oceans* **119**, 2238–2262.
- Zweng, M., Reagan, J., Seidov, D., Boyer, T., Locarnini, R.A., Garcia, H., Mishonov, A., et al., 2018. World ocean atlas 2018, volume 2: salinity. In: Mishonov, A. (Tech. Ed.), *NOAA Atlas NESDIS 82*. Silver Spring, Maryland, NOAA, 50 pp.